Chemical Geology 692 (2025) 122956

Contents lists available at ScienceDirect

Chemical Geology

journal homepage: www.elsevier.com/locate/chemgeo

Research Paper

$^{87}Sr/^{86}Sr$ of Ca-sulfates and water in Atacama Desert as tracer for Ca sources and hydrological distribution processes

Katharina Deußen *, Carsten Münker, Michael Staubwasser

Universität zu Köln, Institut für Geologie und Mineralogie, Zülpicher Str. 49b, 50674 Cologne, Germany

ARTICLE INFO

Editor: Claudia Romano

Keywords:
Gypsum
Evaporites
Sr isotopes
Atacama Desert
Transport processes

ABSTRACT

The Atacama Desert, known as the driest region on Earth, has accumulated substantial salt deposits owing to hyperarid conditions prevailing since the Miocene. These salt deposits mainly include Ca-sulfates and halite, but are also known for their large nitrate deposits. This study focuses on the sources of Ca-sulfates, which occurs in a great mineralogical and compositional diversity. Previous research argued that main sources contributing sulfate to the Atacama salt budget include secondary atmospheric sulfate and biologically recycled sulfate. Secondary atmospheric sulfate originates mostly from marine and atmospheric sources. Additionally, sources delivering Ca into the Atacama Desert include weathered material from the Andes, which is transported by rivers and groundwater flow into the Central depression and to a somewhat lesser extent also marine aerosols. However, there are still open issues, in particular with respect to the elemental mass balances of Ca and sulfur that are different because of contrasting relative abundances in seawater derived components and weathering products. This study uses $^{87}Sr/^{86}Sr$ isotope compositions of both lacustrine as well as pedogenic Ca sulfates and water samples to further investigate sources and transport pathways of Ca within the Atacama Desert. Two case studies from the driest portion of the Atacama Desert, namely the Tiliviche basin (−19.5°S) and the Quillagua-Llamara-Basin (−21.5°S), are investigated in detail. The sulfate samples and their detrital impurities were dissolved utilizing a newly developed method for selective digestion of Ca-sulfates, using anion exchange resin. This method allows for rapid dissolution of Ca-sulfate samples without affecting inherent siliciclastic material. The water samples analyzed exhibit a moderately radiogenic range in $^{87}Sr/^{86}Sr$ of ~0.7063 to ~0.7075. Fossil salar Ca-sulfates display less variation, ranging from ~0.7065 to ~0.7072, whereas pedogenic samples diverge toward higher values, spanning a range from ~0.7067 to ~0.7081. Siliciclastic particles, incorporated within the Ca-sulfates, span a wider $^{87}Sr/^{86}Sr$ range from ~0.7058 to ~0.7095.

The relatively narrow $^{87}Sr/^{86}Sr$ range of the water samples contrasts with the variable Sr isotope composition of the Andean basement. This observation is attributed to mixing and efficient pooling, arising from larger scale water-rock interaction with diverse geological units. The even narrower range observed for lacustrine Ca-sulfate samples likely results from additional homogenization processes, both laterally and vertically, driven by erosion and dissolution-reprecipitation of Ca-sulfates and other salts. In marked contrast, pedogenic Ca-sulfate samples diverge to more radiogenic Sr isotope values. This reflects more local patterns and is indicative for the presence of a high-$^{87}Sr/^{86}Sr$ endmember other than sea spray. In the two case studies investigated, Jurassic limestones in the Coastal Cordillera appear as plausible high-$^{87}Sr/^{86}Sr$ sources. Moreover, the $^{87}Sr/^{86}Sr$ composition of water sources and fossil salar Ca-sulfates in the Tiliviche basin allows identifying past hydrologic networks with different catchments. For example, $^{87}Sr/^{86}Sr$ ratios of fossil lacustrine Ca-sulfates and recent water courses in the Tiliviche basin indicate a former hydrologic connection between two different drainage systems, the Tana/Tiliviche drainage and the Aroma drainage.

1. Introduction

The Atacama Desert stands as Earth's driest region, receiving only 0–5 mm of precipitation per year in its hyperarid core. Paleoclimate studies indicate that hyperarid conditions prevailed since the Miocene (e.g., Jordan et al., 2014; Rech et al., 2003; Risacher and Fritz, 2009).

* Corresponding author.
E-mail address: k.deussen@uni-koeln.de (K. Deußen).

https://doi.org/10.1016/j.chemgeo.2025.122956
Received 13 September 2024; Received in revised form 30 June 2025; Accepted 5 July 2025
Available online 12 July 2025
0009-2541/© 2025 The Authors. Published by Elsevier B.V. This is an open access article under the CC BY license (http://creativecommons.org/licenses/by/4.0/).

This prolonged aridity has resulted in the formation of substantial deposits of water-soluble evaporites, predominantly Ca-sulfates and halite.

One of the primary contributors to the Atacama salt budget are marine aerosols, i.e., sea spray and coastal fog, which predominantly carry sulfates, chlorides and moisture, but also some dissolved cations like Ca or Sr. In particular the moisture content triggers dissolution-reprecipitation processes in the soil (e.g., Rech et al., 2003, Voigt et al., 2020, Klipsch et al., 2023). Locally, unique soil features in the Atacama Desert can be observed, including polygonal patterned ground structures, believed to result from volume changes during sulfate dissolution-precipitation (Ericksen, 1981; Zinelabedin et al., 2024).

The altitude of the coastal fog layer is an essential parameter for sulfate precipitation, as it is restricted by the marine boundary layer (MBL), a robust thermal inversion layer resulting from the convergence of a cold air layer above the ocean with descending warm air. The descending warm air is a consequence of the typical Hadley circulation patterns in subtropical regions (Serpetzoglou et al., 2008; Garreaud et al., 2007; Wood et al., 2011). The cold air above the sea surface is caused by upwelling of the cold Humboldt current along the South American coast (Thiel et al., 2007). The maximum height of the MBL at around 20°S fluctuates between 750 and 1300 m. Common westerly wind systems can carry the moisture through the Coastal Cordillera into the Central Depression to altitudes higher than that of the MBL. However, most parts of the marine aerosols are already blocked at altitudes above 1000 m (Del Rio et al., 2018, 2021). In the northern part of the Central Depression (between 19 and 22°S), fog can penetrate deeper inland compared to the southern part, as the Coastal Cordillera is generally lower and additionally intersected by deeper canyons (quebradas). In the following discussion, we consider the altitudinal range between 225 and 1075 m as influenced by marine fog, following Consentino et al., 2015.

Weathered material from the Andes also plays a major role in the Atacama Desert's salt mass balance. Dissolved ions are primarily transported through groundwater flow and limited surface water runoff. Additionally, dust material can be transported to the Central Depression by easterly winds, which may result from a southward shift of the Bolivian high (Reyers et al., 2019).

Atmospheric deposition is another mechanism for delivering mainly nitrates and sulfates. The sulfates can be emitted into the atmosphere as primary, oxidised atmospheric sulfate (PAS) or in its reduced form as sulfide (secondary atmospheric sulfate – SAS). PAS originate from sea spray or mineral dust from sulfate bearing surface soils and sediments. SAS originates also from marine sources like H_2S or dimethylsulfide (DMS) and from globally distributed volcanic and anthropologic emissions. Secondary oxidation is driven by ozone and other oxidants like -OH radicals or O_2 (Bao et al., 2004; Brimblecombe, 2013; Gamboa et al., 2019; Michalski et al., 2004; Pérez-Fodich et al., 2014). Stable isotope compositions of sulfur and oxygen in sulfates demonstrate that the major amount of atmospheric sulfate is the product of secondary oxidation (Klipsch et al., 2023). The recycling of salts is another process impacting the salt budget. This can occur through aeolian erosion of primary (lacustrine) evaporites, or through dissolution and reprecipitation driven by groundwater flow (brine recycling) (Risacher et al., 2003).

Various geochemical tracers, including element ratios (e.g., Na/Cl, e.g., Voigt et al., 2020) and isotope patterns ($^{87}Sr/^{86}Sr$, $\delta^{18}O_{SO4}$, $\Delta^{17}O_{SO4}$, $\delta^{34}S_{SO4}$, $^{129}I/I$, $\delta^{53/52}Cr$, $\delta^{15}N$) are helpful in distinguishing the different salt sources in the Atacama Desert. For instance, a combination of $\delta^{15}N$, $^{129}I/I$ and $\delta^{53}Cr$ have been utilized to characterize the source of nitrates in the Atacama Desert (Böhlke et al., 1997; Pérez-Fodich et al., 2014). The stable isotope composition of sulfate ($\delta^{18}O_{SO4}$, $\Delta^{17}O_{SO4}$, $\delta^{34}S_{SO4}$) and radiogenic Sr isotopes ($^{87}Sr/^{86}Sr$) were typically employed to identify the sources of Ca-sulfates and other sulfate minerals (e.g., Consentino et al., 2015; Consentino and Jordan, 2017; Gamboa et al., 2019; Klipsch et al., 2023; Rech et al., 2003). Here, stable sulfur isotopes are indicative for the origin of the sulfate, whereas $^{87}Sr/^{86}Sr$ indicate the Ca source. The similar geochemical behavior of Sr and Ca leads to their coupled transport. As, unlike Rb, Sr readily incorporates into the crystal lattice of Ca-sulfates, the Sr isotopic ratio of the source material is frozen in Ca-sulfate without significant radiogenic ingrowth.

Calcium sulfates in the Atacama Desert exhibit remarkable diversity in their morphology and origins. Primary Ca-sulfates form through the evaporation of brines, primarily in lacustrine salar systems that receive water from precipitation in the high Andes via groundwater aquifers and river systems downwards into the Central Depression (e.g., Ericksen, 1981, 1983; Jordan et al., 2022). Often, these lacustrine Ca-sulfates have been transformed to anhydrite. Another variety of primary Ca-sulfates occurs as vein-filling selenites, resulting from subsurface brine circulation and associated evaporation. Moreover, primary Ca-sulfates of marine origin are present, mainly on coastal sections like the Mejillones Peninsula, north of Antofagasta that once formed as a lagoonal system during the Pliocene (Di Celma et al., 2014).

Due to weathering and redeposition processes, secondary gypsum and anhydrite are also present in the Atacama Desert, and are referred to as pedogenic Ca-sulfate below. The source of pedogenic Ca-sulfate was highly debated (Ericksen, 1981 and references therein, from 1861 to 1980), proposing various origins including 1) marine aerosols (Chong, 1988; Ericksen, 1981; Van Moort, 1985), 2) dry and wet deposition of atmospheric aerosols (Böhlke et al., 1997; Claridge and Campbell, 1968; Ericksen, 1981), 3) weathering of Andean volcanics, releasing sulfates and chlorides (Berger and Cooke, 1997; Ericksen, 1961, Ericksen, 1983; Searl and Rankin, 1993), and 4) direct deposition of volcanic sulfides (Berger and Cooke, 1997; Searl and Rankin, 1993). Ongoing research, such as studies conducted by Arens et al., 2021, Consentino et al., 2015, Klipsch et al., 2023, Leybourne et al., 2013 and Voigt et al., 2020, continues to investigate and discuss these different origins.

Rech et al., 2003 pioneered in the use of Sr isotopes to trace the origin of Ca in the pedogenic salt deposits of the Atacama Desert, complemented by stable sulfur isotopes ($\delta^{34}S$), to infer the origin of sulfur. These workers analyzed samples collected along transects stretching from the Coastal Cordillera, affected by sea spray, to the hyperarid core of the Atacama Desert. Their samples covered transects from the Coastal Cordillera to the hyperarid core revealing a binary mixture for both isotope systems with two primary contributors to pedogenic Ca-sulfates: marine sea spray ($^{87}Sr/^{86}Sr = 0.7091$; $\delta^{34}S = +20.9$ ‰) and Andean weathering (mean $^{87}Sr/^{86}Sr = 0.70749$; $\delta^{34}S = +5.4$ ‰). The latter mean value was calculated as a mean of sampled salar waters and evaporites.

This pioneering study was recently expanded by Klipsch et al., 2023, who reported combined isotope analyses for calcium and sodium sulfates (thenardites) for $\delta^{34}S$, $^{87}Sr/^{86}Sr$, $\Delta^{17}O_{SO4}$, and $\delta^{18}O_{SO4}$. The mixing endmembers defined by these tracers include SAS, SAS sourced by dimethylsulfide, biologically recycled sulfate, marine PAS and also hydrothermal sulfur. A novel triple oxygen isotope method was developed to discriminate sulfate ions sourced by the atmosphere and to qualitatively estimate the degree of biological sulfur cycling, which is again dependent on water availability. Worth noticing is the isotope signature of thenardites, which points to a hydrothermal endmember that has not been characterized previously.

With respect to possible Ca sources, Andean basement rocks exhibit a large $^{87}Sr/^{86}Sr$ variability (e.g., Wörner et al., 1992; Lucassen et al., 1999; Kramer et al., 2005; Mamani et al., 2005) which is inherited by interacting ground and surface waters. Therefore, disentangling the different Ca sources using Sr isotopes becomes more complex and applying a mean $^{87}Sr/^{86}Sr$ value for Andean weathering, as proposed by Rech et al., 2003, may be somewhat simplified. Nevertheless, it is now possible to utilize the $^{87}Sr/^{86}Sr$ compositions of salt deposits and their potential source waters to reconstruct the recharge areas and hydrologic networks over time.

This study focuses on the different possible Andean endmembers for Ca supply to the Central Depression. Additionally, the processes of redistribution and sedimentation within the Atacama Desert are

examined, both in spatial and temporal context. We introduce a new analytical protocol that permits separate $^{87}Sr/^{86}Sr$ analyses of highly water-soluble fractions, sulfates and detrital components from the same samples. A comprehensive study was conducted here, producing a dataset comprising approximately 120 samples, mainly sulfates and water. In detail, this dataset includes samples of Ca-sulfates from salars and marine settings, pedogenic Ca-sulfates, as well as the highly water-soluble fraction like halites and thenardites. Furthermore, the siliciclastic components incorporated within the Ca-sulfate deposits are analyzed for comparison.

2. Study area & samples

2.1. The Atacama Desert

The Atacama Desert covers a coastal region in southern Peru and northern Chile between 15° to 30° south and is flanked to the east by the Andean mountain range, with an elevation gradient up to 3500 m above sea level (a.s.l.). The desert owes its unique features to the subduction of the Nazca plate beneath the South American plate since the Jurassic, which has given rise to various episodes of volcanism, compression-related faulting and extension (e.g., Coira et al., 1982; Ramos, 2009; Stern, 2004; Suarez, 2009; Trumbull et al., 2006).

From west to east, the Atacama Desert can be divided into five geologic-topographical units. The Coastal Cordillera, adjacent to the Pacific, shows elevations mainly below 2000 m a.s.l. The basement is composed of batholiths and andesitic volcanic rocks from the Jurassic to early Cretaceous magmatic arc, along with marine limestone, shales, conglomerates (Allmendinger and Gonzales, 2010) as well as widespread Neogene gravels (Vásquez et al., 2018). Adjacent to the Coastal Cordillera, the Central Depression encompasses the hyperarid core of the Atacama. This fore-arc basin is filled with Cenozoic fluvial and lacustrine sediments as well as alluvial fan deposits from both the Precordillera and the Coastal Cordillera (Hartley et al., 2000; Hartley and Evenstar, 2010). The Precordillera, also called Domeyko Cordillera, is a moderately elevated mountain range reaching heights between 3500 and 4000 m a.s.l. It consists of sediments as well as igneous and metamorphic rocks of Paleozoic to Mesozoic age (Victor and Oncken, 2004; Garcia and Herail, 2005). Further east, the Altiplano, an endorheic intramontane basin located at approximately 3600 m, features several sizable salars such as the Salar de Huasco and the Salar de Uyuni. Adjacent to the Altiplano is the volcanically active Western Cordillera, with average altitudes between 3800 and 4500 m and peak heights above 6000 m. The basement of this area comprises Precambrian to Early Paleozoic metamorphic rocks as well as Mesozoic sedimentary and volcanic rocks (e.g., Hartley and Evenstar, 2010; Karatson et al., 2012).

The Atacama Desert is known as the driest desert on Earth. While the Central Andes experience arid conditions with 100–400 mm/year precipitation, the Central Depression is hyperarid with only 0–5 mm/year precipitation (DGA, 1987). Moreover, potential evaporation even reaches 2500 mm/year (Risacher and Fritz, 2009). The extreme aridity is attributed to several factors. First, its location in the subtropical high-pressure belt leads to descending air masses that hinder moisture convection (zonal effect). Secondly, the distance from the Amazonia-Atlantic region, a significant source of moisture for southern America, limits the inland transport of moisture (continental effect). Third, the small amounts of Amazonian moisture that manage to reach inland areas are blocked by the Andes (rainshadow effect). Lastly, the upwelling of the cold Humboldt Current along the western coast of South America cools the air masses in the marine boundary layer, reducing the moisture capacity (oceanic effect) (e.g., Houston and Hartley, 2003).

2.2. Soils in the Atacama Desert

A conceptual soil profile tailored for the nitrate mining regions of the Atacama Desert was developed by Ericksen, 1981 and is depicted in Fig. 1 The uppermost layer, known as *Chuca*, spans a depth of 10 to 30 cm and is composed of powdery to loosely cemented gypsum and anhydrite ($CaSO_4{*}2H_2O$ and $CaSO_4$, respectively), interspersed with varying quantities of silt, sand, and gravels. The *Chuca* layer contains surface and subsurface concretions of diverse sizes and solidification grades, locally referred to as *Losas* (Arens et al., 2021). Often, the *Chuca* layer is overlain by a thin gypsiferous crust of less than 0.5 cm in thickness and a < 20 cm thick layer of highly soluble salts may occur in the lower part. These salts may include thenardite (Na_2SO_4), bloedite ($Na_2Mg[SO_4]_2{\cdot}4H_2O$), epsomite ($MgSO_4$), and humberstonite ($K_3Na_7Mg_2[NO_3|(SO_4)_3]2{\cdot}6H_2O$) (Ericksen, 1981, 1983). The *Chuca* layer gradually evolves into the *Costra* layer, extending 0.5 to 2 m deep and comprising both gypsum and anhydrite. Below the *Costra*, the *Caliche* layer includes firmly cemented halite (NaCl) that occasionally harbors veins and layers of economically important nitratine ($NaNO_3$). At the base of the soil profile, either the *Conjelo*, a regolith cemented

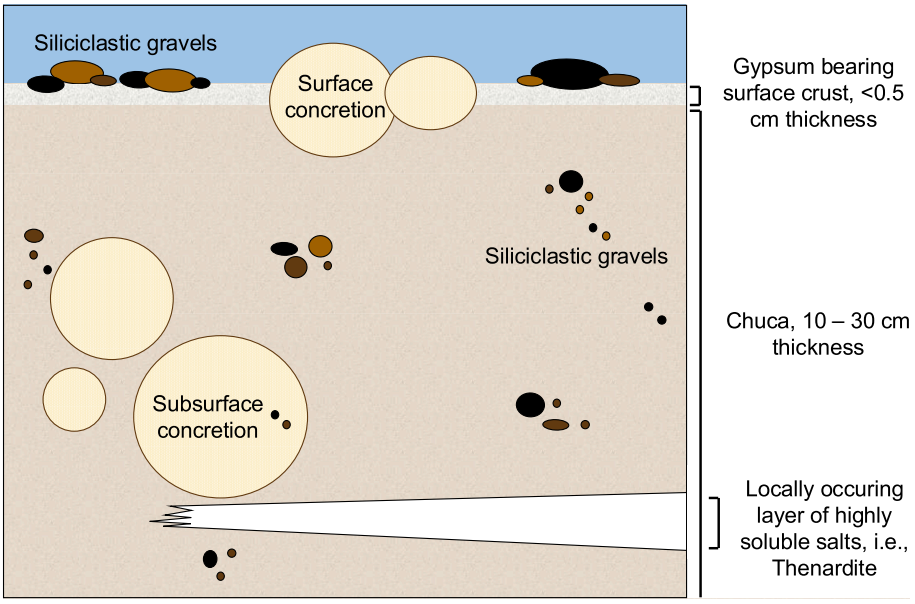

Fig. 1. Schematic sketch through typical uppermost section of the Atacama Desert soil examined here.

Table 1
Sample list, description, location and $^{87}Sr/^{86}Sr$ results. Data is first sorted by sample type, then by latitude.

Sample ID	Description	Location	Latitude [°]	Longitude [°]	Elevation [m]	$^{87}Sr/^{86}Sr$	+/-
Water samples							
ATA19–045	River water, Quebrada Tana	Tiliviche area, Domeyko Cordillera, Camina	−19.4112	−69.6156	1792	0.706422	14
ATA22-W1	River water, Tiliviche river	Tiliviche area, Coastal Cordillera, Huara	−19.5524	−70.1944	55	0.706373	9
ATA18-014a	Groundwater sample from 18 m deep well	Tiliviche area, Domeyko Cordillera, Antofagasta region	−19.6752	−69.9390	1137	0.706676	9
ATA19–046	River Water, Quebrada Aroma	Tiliviche area, Central Depression, Huara	−19.8069	−69.6780	1280	0.707457	12
ATA17–066	River water sample in the middle of a wide flow channel, Quebrada Aroma	Tiliviche area, Quebrada Aroma. Central Depression, Huara	−19.8499	−69.6977	1211	0.707450	8
ATA22–001 water	Salar water, Salar de Huasco	Altiplano, Pica	−20.3000	−68.8477	3789	0.706164	9
ATA14-012d	Groundwater which feeds the Salar de Llamara, sampled from a well	QLB, Salar de Llamara. Central Depression, Pozo Almonte	−21.2722	−69.6179	760	0.707164	17
ATA19–050	River water, Rio Loa	QLB, Central Depression, Quillagua border	−21.6586	−69.536	805	0.707217	13
ATA22-068 A	Hydrothermal water, El Tatio Geysir	Altiplano, Calama	−22.3356	−68.0129	4290	0.708723	17
ATA18–122	Groundwater sample taken from well	Domeyko Cordillera, Sierra Gorda	−23.7885	−69.3510	1720	0.707214	11
PozoAlcayaga	Groundwater, well	Central Depression, Antofagasta	−24.0452	−69.7980	976	0.706101	12
POZO-AB-6	Groundwater, well	Central Depression, Antofagasta	−24.1070	−69.9081	1048	0.706584	14
ATA17-021a	Pond 1 from recent flooding surface with a few trenches cutting older lake sediments	Domeyko Cordillera, Antofagasta region	−24.1185	−68.7183	2984	0.707079	12
ATA17-022a	Pond 3, same flooding surface	Domeyko Cordillera, Antofagasta region	−24.1261	−68.7218	2985	0.707124	8
ATA17-024a	Pond 5, same flooding surface	Domeyko Cordillera, Antofagasta region	−24.1808	−68.7769	2975	0.707136	12
ATA22-W2	Groundwater, spring	Domeyko Cordillera, Taltal	−24.9841	−69.3217	2947	0.707377	10
ATA23–031/1	Groundwater, well	Domeyko Cordillera, Taltal	−24.9900	−69.3200	2966	0.707392	9
Pedogenic samples							
ATA17-086 A	Surface concretion	Tiliviche area, Central Depression, Huara	−19.4464	−69.9759	1090	0.707239	9
ATA17-086B	Sub-surface concretion	Tiliviche area, Central Depression, Huara	−19.4464	−69.9759	1090	0.707228	9
ATA17-086b RESIN	Sub-surface concretion	Tiliviche area, Central Depression, Huara	−19.4464	−69.9759	1066	0.707238	10
ATA19-044C	Sub-surface concretion	Tiliviche area, Central Depression, Camina	−19.4505	−69.6642	1728	0.707086	10
ATA17-087 A	Surface concretion	Tiliviche area, Central Depression, Huara	−19.4729	−69.8818	1186	0.707255	13
ATA17-083B	Sub-surface concretion	Tiliviche area, Coastal Cordillera, Huara	−19.4804	−70.0605	1077	0.707276	10
ATA17-080d H2O	Sub-surface concretion	Tiliviche area, Coastal Cordillera, Huara	−19.5155	−70.1440	965	0.707746	12
ATA17-080d RESIN	Sub-surface concretion	Coastal Cordillera, Huara	−19.5155	−70.1440	965	0.707746	13
ATA19-041 A	Surface concretion	Central Depression, Huara	−19.5639	−69.8584	1199	0.707168	8
ATA19-041B1	Surface, slightly consolidated gypsum chips	Central Depression, Huara	−19.5639	−69.8584	1199	0.708149	24
ATA19-041C	Sub-surface concretion	Central Depression, Huara	−19.5639	−69.8584	1199	0.707146	11
ATA22–12	Surface concretion	Coastal Cordillera, Huara	−19.7244	−70.0843	1165	0.707980	9
ATA19–088	Surface concretion	Central Depression, Pozo Almonte	−20.9948	−69.2751	1444	0.708114	10
ATA22–05	Surface concretion	Central Depression, Pozo Almonte	−21.0056	−69.6964	896	0.707575	11
ATA22–10	Surface concretion	Coastal Cordillera, Iquique	−21.0858	−69.9498	730	0.707762	9
ATA19-095 A	Chuca; Loose material around concretions, 5–15 cm depth	Central Depression, Pozo Almonte	−21.0967	−69.6672	905	0.707552	15
ATA19-095B	Subsurface concretion	Central Depression, Pozo Almonte	−21.0967	−69.6672	905	0.707511	13
ATA22-02B	Surface Chuca	Coastal Cordillera, Iquique	−21.1704	−70.0863	126	0.708094	7
ATA17–153	Chuca and concretions (no depth information)	QLB, Cerro Soledad, Central Depression, Pozo Almonte	−21.2511	−69.5563	1020	0.707329	17
ATA17–151	Surface concretions	QLB, Cerro Soledad, Central Depression, Pozo Almonte	−21.2541	−69.5554	1053	0.707224	11
ATA22–29 A	Surface crust	QLB, Central Depression, Pozo Almonte	−21.2706	−69.6625	764	0.706871	10
ATA22–29B	Subsurface concretion	QLB, Cerro Soledad, Central Depression, Pozo Almonte	−21.2706	−69.6625	764	0.707047	7
ATA19-077B	Subsurface concretion	Central Depression, Maria Elena	−22.2675	−69.4351	1345	0.706866	12
ATA19–076 B	Sand cemented with gypsum, 5–30 cm depth	Central Depression, Maria Elena	−22.2711	−69.3541	1500	0.706748	21
ATA19–076c H2O	Surface chuca (< 5 cm depth)	Central Depression, Maria Elena	−22.2711	−69.3541	1500	0.706815	9
ATA19–076c RESIN	Surface chuca (< 5 cm depth)	Central Depression, Maria Elena	−22.2711	−69.3541	1500	0.706821	21
ATA19-078B	Sub-surface concretion	Central Depression, Maria Elena	−22.2780	−69.5093	1200	0.706866	11
ATA19-082B	Sub-surface concretion	Central Depression, Maria Elena	−22.2811	−69.6922	1235	0.707044	12
ATA17-014a	Chuca, 5–10 cm depth	Central Depression, Antofagasta	−23.3176	−70.5328	1255	0.707347	–
ATA17-014B	Subsurface concretion	Central Depression, Antofagasta	−23.3176	−70.5328	170	0.707351	15
ATA18-121b	Thenardite	Domeyko Cordillera, Antofagasta	−23.7764	−69.3902	1771	0.707002	12
ATA17-016a	Surface Chuca	Central Depression, Antofagasta	−23.8877	−69.8164	790	0.707622	–
ATA17-020a	Surface Chuca	Domeyko Cordillera, Antofagasta	−24.1166	−68.7020	3109	0.707265	–
ATA17-026b	Subsurface concretion, 10 cm depth	Domeyko Cordillera, Antofagasta	−24.1864	−69.2873	2187	0.707464	50
ATA18-001c	Thenardite	Central Depression, Antofagasta	−24.3271	−69.9617	1299	0.706910	10
ATA22–15	Thernadite	Central Depression, Antofagasta	−24.3272	−69.9616	1303	0.706923	9
ATA18-126a	Surface crust	Central Depression, Taltal	−25.0672	−69.9970	1920	0.707369	11
ATA18-126b	Thenardite	Central Depression, Taltal	−25.0672	−69.9970	1920	0.707336	14
ATA18-126C	Subsurface, Chuca, 30 cm depth	Central Depression, Taltal	−25.0672	−69.9970	1920	0.707366	11
ATA18-125a	Surface Chuca, 5 cm depth	Central Depression, Taltal	−25.1384	−69.9180	1809	0.707089	13
ATA18-125b	Thenardite	Central Depression, Taltal	−25.1384	−69.9180	1809	0.707082	9

(*continued on next page*)

Table 1 (*continued*)

Sample ID	Description	Location	Latitude [°]	Longitude [°]	Elevation [m]	$^{87}Sr/^{86}Sr$	+/-
ATA18-125c	Subsurface concretion	Central Depression, Taltal	−25.1384	−69.9180	1809	0.707094	12
Lacustrine Ca-sulfate samples							
ATA18-022a	Halite crust	Tiliviche area, Coastal Cordillera, Huara	−19.4814	−70.0529	1007	0.706946	16
ATA18-022b	Sulfate / Gypsum. Transition, lake become salt flat	Tiliviche area, Pampa Tiliviche, Central Depression, Huara	−19.4814	−70.0529	1007	0.706897	10
ATA18-012d	Gypsum/ Tiliviche, lake become salt flat	Tiliviche area, Pampa Tiliviche, Central Depression, Huara	−19.5041	−69.9617	1085	0.706544	15
ATA18-025b-c	Selenite. Transition, lake become salt flat	Tiliviche area, Pampa Tiliviche, Central Depression, Huara	−19.5627	−70.1185	1181	0.706527	8
ATA18-015a	Gypsum	Tiliviche area, Coastal Cordillera, Huara	−19.6792	−70.0209	1134	0.707069	11
ATA22–42 H2O	Gypsum	Coastal Cordillera, Iquique	−21.2027	−69.9070	852	0.706843	11
ATA22–42a RESIN	Gypsum	Coastal Cordillera, Iquique	−21.2027	−69.9070	852	0.706822	8
ATA17–159	Lowest bank of halite/sulfate breccia	Level 2 of Cerro Soledad, Central Depression, Pozo Almonte	−21.2443	−69.5586	808	0.706894	11
ATA17–156	Massive sulfate with visible crystals, possibly gypsum, looks like secondary crystals.	Level 4 of Cerro Soledad, Central Depression, Pozo Almonte	−21.2492	−69.5588	951	0.706802	16
ATA17–155	Halite with anhydrite veins /	Level 5 (uppermost) of Cerro Soledad, Central Depression, Pozo Almonte	−21.2496	−69.5573	984	0.706879	16
ATA17–158	Massive halite with large sulfate clasts	Level 3 of Cerro Soledad, Central Depression, Pozo Almonte	−21.2507	−69.5605	899	0.706817	19
ATA22–29-3 F&G H2O	Gypsum	Coastal Cordillera, Pozo Almnote	−21.2706	−69.6625	763	0.706858	18
ATA22–29-3 F&G H2O	Gypsum	Coastal Cordillera, Pozo Almnote	−21.2706	−69.6625	763	0.706858	18
ATA22–29-3 F&G RESIN	Gypsum	Coastal Cordillera, Pozo Almnote	−21.2706	−69.6625	763	0.706847	9
ATA22–29-3 F&G RESIN	Gypsum	Coastal Cordillera, Pozo Almnote	−21.2706	−69.6625	763	0.706847	9
ATA17–130	Recent gypsum precipitate	QLB, Salar de Llamara, Central Depression, Pozo Almonte	−21.3521	−69.5610	754	0.707196	10
ATA17–168	Selenite	QLB, Level 5 (uppermost) of Cerro Soledad, Central Depression, Pozo Almonte	−21.3529	−69.5603	817	0.706880	13
ATA17-169b	Halite in which the selenite grew	QLB, Level 5 (uppermost) of Cerro Soledad, Central Depression, Pozo Almonte	−21.3529	−69.5603	795	0.707206	13
ATA19–064	Selenite	QLB, Rio Loa Canyon*, Central Depression	−21.4461	−69.7568	811	0.707137	14
ATA22–53-R1 Selenite H2O	Gypsum	QLB, Rio Loa Canyon*, Central Depression	−21.4462	−69.7572	811	0.706672	10
ATA22–53-R1 Selenite RESIN	Gypsum	QLB, Rio Loa Canyon*, Central Depression	−21.4462	−69.7572	811	0.706657	10
ATA19–066	Selenite	QLB, Rio Loa Canyon*, Central Depression	−21.4463	−69.7569	811	0.706677	13
ATA17–038	Selenite	QLB, Rio Loa Canyon*, Central Depression	−21.4466	−69.7568	811	0.706686	14
ATA19–067	Selenite	QLB, Rio Loa Canyon*, Coastal Cordillera	−21.4486	−69.7562	824	0.706695	15
ATA19–073	Gypsum	QLB, Rio Loa Canyon*, Central Depression	−21.4566	−69.7315	816	0.706777	13
ATA17–037	Selenite	QLB, Rio Loa Canyon*, Central Depression	−21.4612	−69.7023	821	0.706691	14
ATA18-009a	Selenite, top	QLB, Rio Loa Canyon*, Central Depression	−21.6271	−69.5496	811	0.706644	16
ATA18-009b	Selenite, middle	QLB, Rio Loa Canyon*, Central Depression	−21.6271	−69.5496	811	0.706615	14
ATA18-009c	Selenite, bottom	QLB, Rio Loa Canyon*, Central Depression	−21.6271	−69.5496	811	0.706811	10
ATA18-004b	Gypsum interlayed with alluvial fan material, 25–30 cm	Precordillera, Taltal	−24.9015	−69.2691	2943	0.707172	12
ATA18-004c	Gypsum interlayed with alluvial fan material, 65–70 cm	Precordillera, Taltal	−24.9015	−69.2691	2943	0.707128	11
ATA22–018	Gypsum layer above lake sediments and below Miocene ignimbrite, polyphase.	Domeyko Cordillera, Taltal	−24.9773	−69.3238	2955	0.706807	10
Lacustrine diatomite samples							
ATA18-022c	Diatomite	Tiliviche area, Central Depression, Huara	−19.4814	−70.0530	1007	0.706784	10
ATA7-073c	Upper Diatomite	Tiliviche area, Central Depression, Huara	−19.5486	−70.0180	1034	0.707017	14
ATA17-073e	Lower Diatomite	Tiliviche area, Central Depression, Huara	−19.5486	−70.0180	1034	0.707013	11
ATA17–040	Diatomite	QLB, Rio Loa Canyon*, Central Depression, Antofagasta	−21.5355	−69.6377	869	0.708526	13

(*continued on next page*)

Table 1 (*continued*)

Sample ID	Description	Location	Latitude [°]	Longitude [°]	Elevation [m]	$^{87}Sr/^{86}Sr$	+/-
ATA17-041a	Diatomite	QLB, Rio Loa Canyon*, Central Depression, Antofagasta	−21.5872	−69.6054	882	0.707280	14
ATA7-041c	Diatomite	QLB, Rio Loa Canyon*, Central Depression, Antofagasta	−21.5872	−69.6054	882	0.706711	11
Travertine alternating with supergene Ca-sulfate							
ATA22-17 A.1	Supergene gypsum	Domeyko Cordillera, Commune Taltal, Region Antofagasta,	−24.8738	−69.5477	2474	0.705985	9
ATA22-17 A.2	Supergene carbonate	"	−24.8738	−69.5477	2474	0.704392	11
Marine gypsum samples							
AT22–65-LL1-A	Marine gypsum, top layer	Mejillones	−23.3200	−70.5328	124	0.708999	11
AT22–65-LL1-E	Marine gypsum, top layer	Mejillones	−23.3176	−70.5328	124	0.709002	9
AT22–65-LL2-A	Marine gypsum, middle layer	Mejillones	−23.3176	−70.5328	124	0.709054	10
AT22–65-LL2-D	Marine gypsum, middle layer	Mejillones	−23.3176	−70.5328	124	0.709054	9
AT22–65-LL3-B	Marine gypsum, top layer	Mejillones	−23.3176	−70.5328	124	0.708965	11
AT22–65-LL3-C	Marine gypsum, top layer	Mejillones	−23.3176	−70.5328	124	0.708964	9

* Rio Loa Canyon refers to a general proximity to the Canyon, not necessarily a position inside the canyon.

with salt, or the C*oba*, an unconsolidated regolith, are present. In this work we examine all different components of the uppermost soil (Fig. 1), including *Chuca, Losas,* thenardite layers, the surface crust and the incorporated siliciclastic components. The majority of samples comprise *Chuca* and *Losas.*

2.3. Sample locations and types

In this work, a comprehensive study on approximately 120 samples was conducted, covering an area between 19° and 25° south (Table 1, Table 1 Appendix). Most of the samples were taken within the Central Depression, with some corresponding to the Coastal Cordillera, Precordillera and Altiplano (Fig. 2). The sample set comprises 19 water samples, 44 pedogenic sulfate samples, six diatomite samples and 33 lacustrine Ca-sulfate samples. Additionally, the study includes 13 samples consisting of siliciclastic material, extracted from Ca-sulfates of different origin (5 lacustrine, 7 pedogenic) as well as the suspended load of the Tiliviche river. Six marine Ca-sulfate samples from Mejillones Peninsula are also included.

The group of water samples includes the Tiliviche and Rio Loa rivers, and wells and springs from the Central Depression and Precordillera. A water sample from the hydrothermal El Tatio Geysir on the Chilean Altiplano marks a hydrothermal endmember.

Pedogenic samples consist primarily of concretions, loose chuca material, and minor amounts of thenardite, largely consistent with those previously described and analyzed by Voigt et al. (2020). As listed in Table S1, "surface samples" refer to materials collected from depths of 0–10 cm, while "subsurface samples" were taken from depths of 10–30 cm.

Based on deposition rates of 5–10 g/m^2/year (Wang et al., 2014) and reported bulk densities for Atacama soils ranging from 1.34 to 1.68 g/cm^3 (Zinelabedin et al., 2024; see also Wang et al., 2014: ~1.4 g/cm^3), the expected sediment accumulation is approximately 0.38–14 μm/year. Accordingly, the 10 cm surface samples likely represent an age range of ~7000 to 26,000 years, while subsurface samples (to 30 cm depth) may reach a maximum age of ~79,000 years.

Thus, the surface samples are interpreted as dating to the Holocene or uppermost Pleistocene, while the subsurface samples represent upper Pleistocene material.

At some sites, in-depth soil profiles were sampled and analyzed, investigating the different soil phases. Generally, these pedogenic samples are not significantly influenced by marine fog (Klipsch et al., 2023; Rech et al., 2003; Voigt et al., 2020).

The six diatomite samples have been taken in the Tiliviche and QLB region. The diatomites document the full lake stage of the QLB system and the Tiliviche lake prior to evaporite deposition. These deposits have been analyzed to characterize the initial lake stages and to identify possible changes of drainage patterns with time.

The 33 lacustrine Ca-sulfate samples include one lacustrine Ca-sulfate specimen which precipitated from an active salar system (Salar de Llamara), along with 32 fossil salar Ca-sulfate samples that primarily originate from the Soledad formation (4.1 to 2.6 Ma; Jordan et al., 2022). The samples were predominantly taken within the Quillagua-Llamara basin (QLB), with a few exceptions from the Tiliviche basin and areas south of the QLB.

The analyzed siliciclastic material was primarily obtained from the siliciclastic detritus incorporated within the Ca-sulfate samples, following the selective dissolution procedure outlined below. Additionally, soil samples virtually entirely composed of siliciclastics, as shown by XRD data (Voigt et al., 2020), were included. One siliciclastic sample represents the suspended load of the Tiliviche river. The six marine Ca-sulfate samples from Mejillones Peninsula were taken from three of a total of six Ca-sulfate layers, each separated by clay layers. According to the geological map of Cortés et al., 2007, this succession is of Pleistocene to Holocene age.

Additionally, one travertine sample alternating with supergene gypsum was analyzed.

3. Methods and selective dissolution protocol

Many Ca-sulfates incorporate varying amounts of detrital components, and their $^{87}Sr/^{86}Sr$ values might deviate from those of the Ca-sulfate itself. Depending on the amount of detritus, the Sr concentrations in both the detritus and the Ca-sulfate, and the difference in the Sr isotope composition, these detrital signals may overprint that of the Ca-sulfates. Therefore, a selective dissolution method that does not affect the detrital components was developed here. In this new approach, anion exchange resin is used to selectively dissolve the water-soluble sulfate minerals. Approximately 50 mg of Ca-sulfate (or more, depending on the actual sulfate content), along with approximately 15 ml of MilliQ water and 750 μl of pre-cleaned anion resin (AG1-X8, 100–200 mesh, BIO-RAD) are placed in a vial and kept at 60 °C for 1–2 days. The anion exchange resin was conditioned with HCl before and rinsed with MilliQ water afterwards to ensure a neutral pH. During the reaction time of 1–2 days, Ca-sulfate (along with other water-soluble minerals) starts to dissolve. The (sulfate) anions get adsorbed onto the resin, lowering the ion activity product of the sulfates in the solution. Consequently, more Ca-sulfate can be dissolved with time and the natural process of Ca-sulfate dissolution in water is accelerated. After 1–2 days, the solution with the dissolved cations is separated from the resin that also

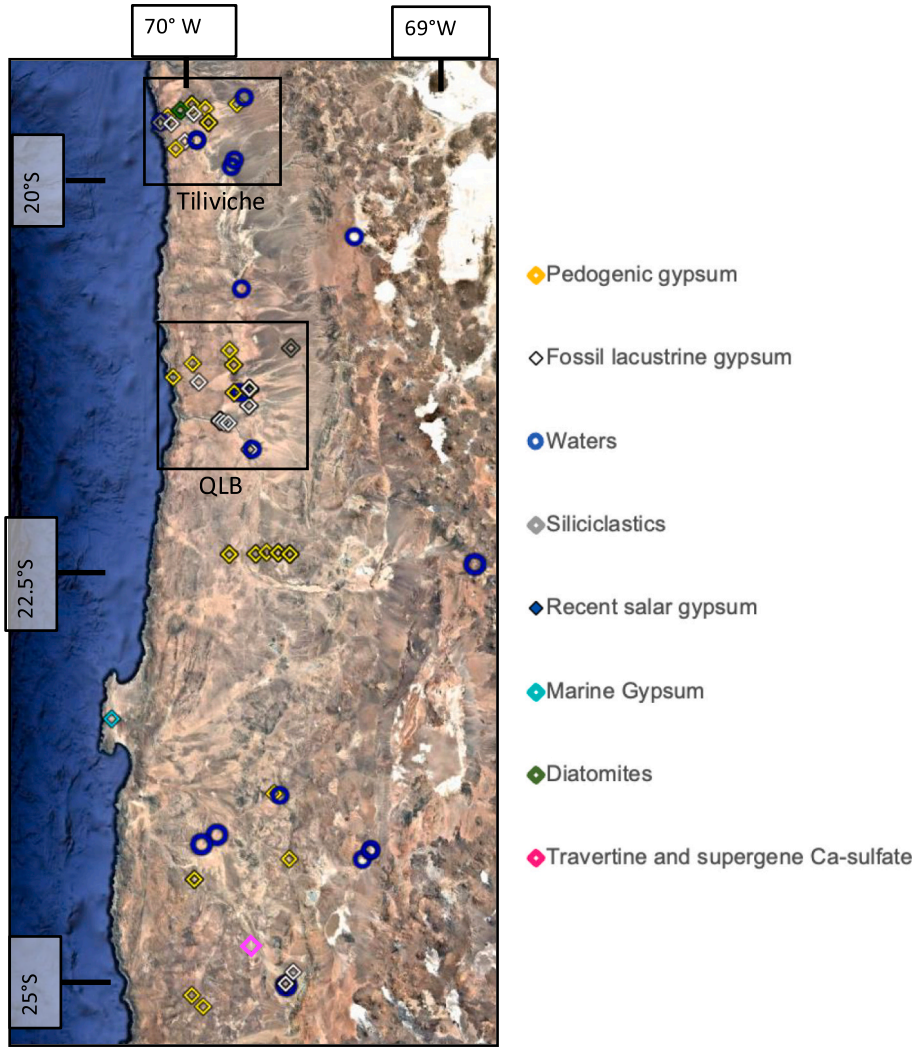

Fig. 2. Map of the study area showing sample locations. The Tiliviche basin and of the Quillagua-Llamara basins (QLB) investigated here in more detail are indicated by the black boxes. Modified from Google Earth (Data SIO, NOAA, U.S. Navy, NGA, GEBCO, Image Landsat / Copernicus).

contains the unaffected residual siliciclastic minerals. Only in some instances, residual gypsum grains have been observed. However, this does not affect the $^{87}Sr/^{86}Sr$ ratio of the solution, as the dissolution process doesn't fractionate radiogenic Sr isotope compositions. After dry-down of the solution, it is taken up in 2.5 N HCl for standard cation column chemistry to separate the Sr. For selected samples, the remaining siliciclastic components were digested and analyzed separately. The digestion process follows a standard protocol for silicates by adding a mixture of concentrated HF-HNO_3, followed by several drydown steps in HNO_3 and total dissolution in 6 M HCl.

To validate this method, we conducted a series of sequential dissolution tests using this protocol. We selected Ca-sulfates from Tiliviche, the Quillaga-Llamara basin and from Tocopilla, known to contain a significant portion of highly water-soluble minerals, as indicated by previous XRD data (Voigt et al., 2020). During the first leaching step, the samples were dissolved in water for approximately 30 min. During this time, the strongly water-soluble minerals like nitratine or halite immediately dissolve. After 30 min, the aqueous solution and the remaining undissolved sample were separated. After thorough rinsing, which is supposed to affect the Ca-sulfate phase just insignificantly due to slow dissolution rates, the residual sample underwent the resin procedure as described above to dissolve the less water-soluble sulfates. The residual sample, comprising the resin and the unaffected siliciclastics, was then digested using the acid procedure described above. All three cuts of the samples were dried down and the Sr purified by column chemistry. The results of these leaching tests are presented in Fig. 5 and are discussed below.

The diatomite samples have been digested with 2.8 N HNO_3 in a first step to digest potentially included carbonates. In a second step, the sample was treated with a mixture of concentrated HF-HNO_3 to digest the SiO_2 phase.

Measurements of $^{87}Sr/^{86}Sr$ were conducted with a Neptune MC-ICP-MS at Cologne. The mass-dependent isotope fractionation observed during measurement was corrected to an $^{86}Sr/^{88}Sr$ value of 0.1194 using the exponential law.

The mass dependent fractionation of $^{87}Sr/^{86}Sr$ was corrected to a $^{86}Sr/^{88}Sr$ value of 0.1194 using the exponential law. Results are given relative to a $^{87}Sr/^{86}Sr$ value of 0.710240 for the NBS 987 standard. Possible interferences were monitored using $^{83}Kr/^{86}Sr$ and $^{85}Rb/^{86}Sr$. The external reproducibility is better than +/ 100 ppm (2s) statt (2).

4. Results

Measured $^{87}Sr/^{86}Sr$ data from this study are shown in Fig. 3. The siliciclastic components in sulfates exhibit a range from ~0.7058 to ~0.7095, with the majority of samples falling between ~0.7063 to ~0.7072. The marine gypsum samples show very similar $^{87}Sr/^{86}Sr$ ratios of ~0.7090 which are slightly less radiogenic than the seawater

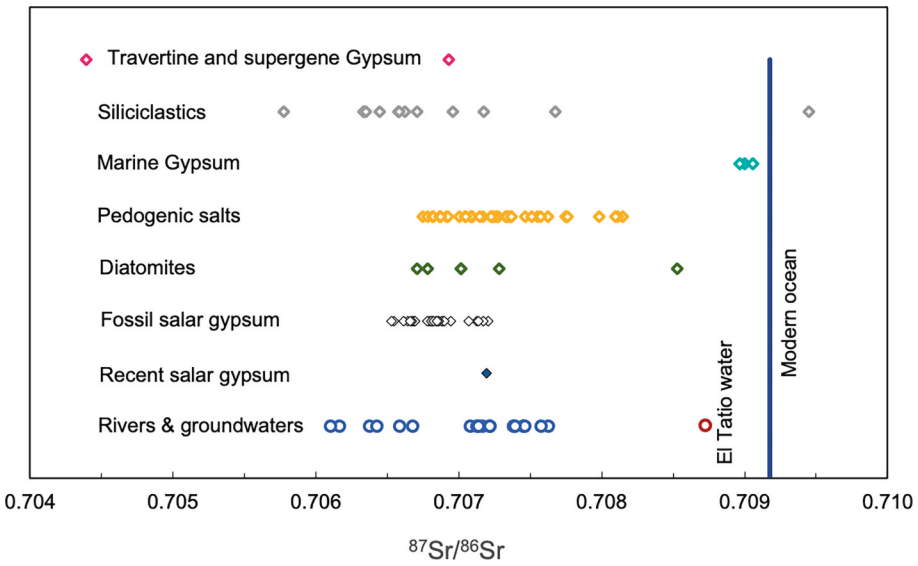

Fig. 3. Overview of $^{87}Sr/^{86}Sr$ compositions of all analyzed samples from the Atacama Desert. Error bars are smaller than symbol sizes.

composition of the time of their formation 1.8 Ma ago (0.709093, McArthur et al., 2020) (refer to section 5.2.1). The fossil salar gypsum samples cover a slightly less radiogenic range from ~0.7065 to ~0.7072. The $^{87}Sr/^{86}Sr$ composition of the single analyzed recent salar gypsum sample falls within the upper range at ~0.7072. The $^{87}Sr/^{86}Sr$ of the river and groundwater water samples range from ~0.7061 to ~0.7075. The hydrothermal El Tatio water exhibits a remarkably radiogenic value of ~0.7087. The diatomites show $^{87}Sr/^{86}Sr$ ratios comparable to the fossil salar gypsum and water samples (~0.7067 to ~0.7073) with one outlier, showing a conspicuously high radiogenic Sr isotope composition of ~0.7085. The large group of pedogenic salt samples is relatively uniform with Sr isotope compositions between ~0.7067 and ~ 0.7081.

For some samples, the $^{87}Sr/^{86}Sr$ of the inherent siliciclastic residues after leaching were also examined, using the above acid digestion protocol (Fig. 4). In a few examples, the $^{87}Sr/^{86}Sr$ of salts, including Ca-sulfates, closely resemble that of the siliciclastic components. However, for most cases, the siliciclastic components show different $^{87}Sr/^{86}Sr$ than the highly soluble salts and the sulfates. In case of the fossil salar Ca-sulfates, the siliciclastic components often exhibit more radiogenic $^{87}Sr/^{86}Sr$ values. Conversely, in the pedogenic Ca-sulfate samples, the inherent siliciclastic material tends to show less radiogenic $^{87}Sr/^{86}Sr$ values.

The travertine sample exhibits the most unradiogenic Sr isotope composition within our data set (~0.7044), while the alternating supergene gypsum shows a Sr isotope composition within the range of the other gypsum types (~0.7069).

5. Discussion

5.1. Selective digestion protocol

A series of selective digestion tests were conducted (Fig. 5) that provide insights into the diagenetic history of the heterogeneously composed sediments in the Atacama Desert. A consistent observation was the remarkable similarity of the Sr isotope composition to that of the water-leached fraction (nitrates, chlorides and thenardites) with that of the resin-leached fraction (other sulfates). In contrast, the siliciclastic components often exhibit significant differences.

From the above-mentioned observations, three conclusions can be drawn. First, the chosen resin method that dissolves both Ca-sulfate and highly water-soluble salts, is suitable for investigating the Sr isotope composition of Ca-sulfates. This is true even for mixed samples with significant amounts of highly water-soluble salts. Here, the siliciclastic components with their different Sr isotope composition apparently remained unaffected and are not leached. Secondly, the experiments also showed that Ca-sulfates are frequently in Sr isotopic equilibrium with the ambient water-soluble salts like halite or thenardite. This isotopic equilibrium might stem from either a shared primary Ca source or, alternatively, from dissolution-reprecipitation processes that homogenize the Sr isotopic budget of the system after crystallization.

As third important conclusion, the siliciclastic components in Ca-sulfate-bearing samples often do not show equilibrium with the evaporite minerals. Studies previously investigating the degree of equilibration between the parent rock and groundwater from which the evaporites precipitate and inherit their $^{87}Sr/^{86}Sr$ signature are Herrera et al., 2018 and Gamboa et al., 2019. Herrera et al., 2018 showed that coastal springs in the Atacama Desert receive minimal contributions from water-rock interaction, with their Sr ion budgets being primarily influenced by atmospheric deposition. In deep groundwater seawater-derived signals are subsequently modified through water-rock interaction and hydrothermal alteration. Waters from deep boreholes show extensive water-rock interaction, as indicated by $^{87}Sr/^{86}Sr$ signatures close to those of the parent volcanic and intrusive rocks. This highlights that the degree of equilibration varies significantly depending on the groundwater type. Likewise, Gamboa et al., 2019 identified distinct geological units influencing the composition of groundwater. Above 3400 m, groundwater flows through fractured Permian volcanic rocks, resulting in short residence times and a low degree of equilibration with bedrock, although some interaction is evident from elevated $^{87}Sr/^{86}Sr$ ratios compared to recharge water. Below 3400 m, groundwater springs indicate a less radiogenic source, consistent with Jurassic marine limestones.

However, these findings, while advancing the understanding of groundwater dynamics, cannot explain the disequilibrium observed between evaporite deposits and embedded siliciclastic grains. This disequilibrium is likely attributed to the distinct sources of Ca-sulfate forming brines and siliciclastic grains. While intra-basinal siliciclastic grains are directly sourced from the underlying bedrock, extra-basinal grains can be transported from the high Andes in the East or the Coastal Cordillera in the West. The brines contributing to the Ca-sulfate itself seem to be of different origin, as indicated by their distinct $^{87}Sr/^{86}Sr$, reflecting different transport mechanisms. Extra-basinal siliciclastic grains and Ca-sulfate-forming Ca ions can both be transported by rarely occurring surface water runoff. However, the siliciclastic grains are also transported by wind, while the Ca-sulfates may also be

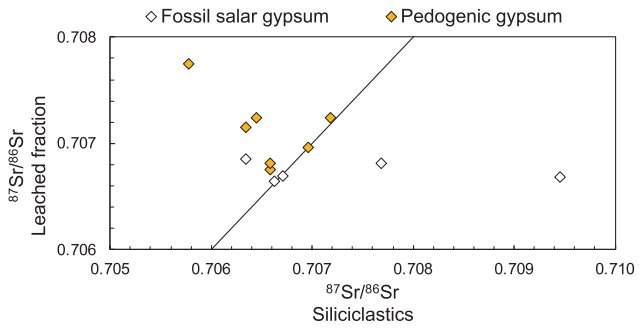

Fig. 4. $^{87}Sr/^{86}Sr$ compositions of the leached sulfate fraction versus the residual siliciclastics. The black line marks the 1:1 ratio (identical values).

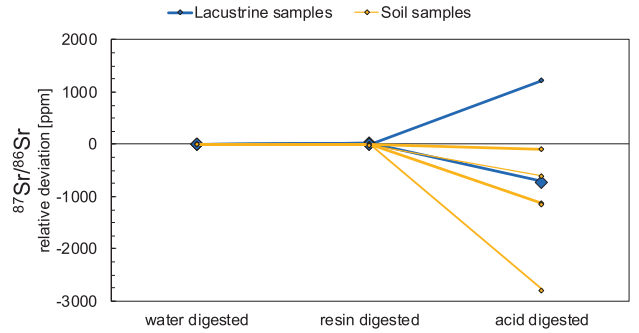

Fig. 5. Results of selective digestion tests showing the relative deviation [ppm] of the $^{87}Sr/^{86}Sr$ isotope composition between the water-leached, the acid-digested fraction and that of the resin leached fraction of different samples.

sourced by groundwater flow. The difference between the $^{87}Sr/^{86}Sr$ of Ca-sulfates and siliciclastic components therefore appears to be maintained after deposition, as there is less chance for subsequent diagenetic equilibration, at least in the dry environment. Siliciclastic components appear to exchange much more slowly with their environment, given the infrequent and sporadic water occurrences.

Previous studies investigating the $^{87}Sr/^{86}Sr$ of pedogenic Ca-sulfate have utilized either acid digestion (Rech et al., 2003) or water dissolution (Consentino et al., 2015; Consentino and Jordan, 2017). Rech et al. (2003) utilized 2 N HCl for sample digestion and reported$^{87}Sr/^{86}Sr$ for pedogenic Ca-sulfate samples ranging from 0.7070 to 0.7076. These values fall within the range observed in the pedogenic samples analyzed in this study and do not provide evidence for significant dissolution of siliciclastics during their analyses. This could be attributed to negligible amounts of siliciclastic material, the presence of HCl-resistant silicates or to similar $^{87}Sr/^{86}Sr$ in siliciclastic particles and pedogenic salts. The latter remains plausible based on some results presented here (see Fig. 5). However, for samples with a high siliciclastic content of different $^{87}Sr/^{86}Sr$ ratios, digestion with HCl may substantially alter the measured $^{87}Sr/^{86}Sr$.

Consentino et al. (2015) and Consentino and Jordan (2017) dissolved their gypsum samples using ultrapure H_2O in an ultrasonic bath. This method eliminates the risk of dissolving silicate minerals. In comparison, however, our resin method offers several benefits: it can dissolve larger amounts of gypsum within a shorter time frame, as the sulfate anions are continuously removed from the solution by the anion resin. Additionally, the same quantity of gypsum can be dissolved in a smaller volume of water. Although the actual dissolution times reported by Consentino et al. (2015) and Consentino and Jordan (2017) are shorter than those typically applied for the resin method, a reduction in dissolution time for the resin method should be feasible with further optimization.

5.2. Endmember characterization

In Ca-sulfates, ratios of $^{87}Sr/^{86}Sr$ are suitable as tracer for the Ca source, but don't provide insight into the transport processes of sulfate. The origin of sulfate in the Atacama Desert was already investigated in several previous studies. In the comprehensive study of Klipsch et al., 2023, a combination of $\delta^{34}S$, $\delta^{18}O_{SO4}$ and $\Delta^{17}O_{SO4}$ has been used. Similar to $^{87}Sr/^{86}Sr$ for Ca, $\delta^{34}S$ reflects the sulfate source with a specific value for marine sulfate ($\delta^{34}S \sim 22‰$). The $\delta^{18}O_{SO4}$ value depends on both the sulfate source and on the oxidation mechanisms. The $\Delta^{17}O_{SO4}$ value quantifies mass-independent oxygen fractionation that takes place during ozone oxygenation of SAS. If the SAS is biologically recycled after deposition, mass-independent anomalies diminish. Thus, $\Delta^{17}O_{SO4}$ serves as a proxy for ozone oxidation and biological cycling, which depends on water availability. Therefore, $\Delta^{17}O_{SO4}$ can practically be used as proxy for hyperaridity (Klipsch et al., 2023). In the Atacama Desert the majority of the accumulated sulfate is of secondary atmospheric origin or results from biologic sulfur cycling (Bao et al., 2004; Brimblecombe, 2013; Gamboa et al., 2019; Klipsch et al., 2023; Michalski et al., 2004; Pérez-Fodich et al., 2014).

This section focusses on $^{87}Sr/^{86}Sr$ as tracer for the origin of Ca ions in sulfates. Values of $^{87}Sr/^{86}Sr$ can be used to define major mixing endmembers contributing Ca to the Ca-sulfate deposits. In the Atacama Desert, these ions may originate from various sources, primarily Andean weathering but also atmospheric sources supplying marine sea spray (e.g., Berger and Cooke, 1997; Ericksen, 1981; Klipsch et al., 2023; Rech et al., 2003; Voigt et al., 2020).

5.2.1. The marine endmember

The present-day $^{87}Sr/^{86}Sr$ signature of the marine endmember mirrors that of the modern ocean, marked at 0.709174 (McArthur et al., 2020). To further investigate the local marine contributions, we examined six marine gypsum samples extracted from three of six distinct gypsum layers on Mejillones Peninsula. Specifically, we analyzed the top, middle and bottom gypsum layers. These deposits originally formed in a lagoonal environment (Di Celma et al., 2014) and were previously dated at ~1.8 Ma using the U/Pb decay system (Münker et al., 2023). The $^{87}Sr/^{86}Sr$ of the marine Ca-sulfate should then be expected to be identical to that of the ambient ocean 1.8 Ma ago (0.709093, McArthur et al., 2020). However, the $^{87}Sr/^{86}Sr$ of the Mejillones gypsum samples are lower than expected (0.70896–0.70905) (Fig. A1). This discrepancy can be best explained by terrigenous components, transported by riverine systems into the shallow coastal waters. The $^{87}Sr/^{86}Sr$ data therefore indicate that the ambient meteoric waters do not immediately homogenize with the ambient ocean. Instead, the meteoric waters alter the Sr isotope budget in the lagoonal system and possibly in the shallow coastal environment. Consequently, the common practice of using Sr isotopes in carbonates or sulfates for direct dating (e.g., Denison et al., 1998; Müller and Mueller, 1991) should be treated with caution, especially for minerals like gypsum formed in restricted environments such as lagoonal settings.

5.2.2. The hydrothermal endmember

To explore the hydrothermal endmember, we examined two travertine deposits that are likely related to hydrothermal outgassing and are located on the Domeyko Cordillera in the Taltal municipality. Additionally, we analyzed hydrothermal water from the El Tatio Geysir near San Pedro the Atacama and thenardite deposits from the Taltal and Antofagasta regions, showing sulfur isotope compositions indicative of hydrothermal origin (Klipsch et al., 2023).

The essential condition for the formation of travertine deposits is the addition of CO_2 gas. This can be sourced either by hydrothermal outgassing or by the digestion and oxidation of organic matter. The latter would require high organic carbon contents in the soil, which is unlikely

for Atacama Desert soils. Hence, we assume a hydrothermal origin of the CO_2 forming the travertines. The travertine deposit studied here intercalates with microcrystalline gypsum. The Sr isotope composition of the travertine marks the lowest value within our entire dataset (~0.7044). In contrast, the microcrystalline gypsum layer display a more radiogenic Sr isotope ratio of ~0.7069, suggesting meteoric water contribution to the parental brine of the Ca-sulfates.

In contrast, the hydrothermal water from the El Tatio geyser exhibits one of the most radiogenic values among our data set ($^{87}Sr/^{86}Sr$ ~ 0.7087). The water originates from meteoric sources, infiltrating the subsoil ~15 km east of El Tatio and is heated and enriched in dissolved species while passing underneath a volcanic chain (Giggenbach, 1978). Its Cl content is high (~5000 to ~8000 mg/L) and $^{87}Sr/^{86}Sr$ values of the hydrothermal solutions known from the literature range between 0.70876 and 0.70896, also overlaping $^{87}Sr/^{86}Sr$ of the dacites found in the central volcanic zone (0.70876 to 0.70896). Another type of water at El Tatio originates from shallower, local groundwater heated by ascending gases, characterized by high concentrations of sulfate rather than chloride (Cortecci et al., 2005; Giggenbach, 1978). Based on the $^{87}Sr/^{86}Sr$ and the high chloride content of the water sample analyzed in this study (>6000 mg/L), the sample belongs to the chloride-rich water type.

The thenardites from the Antofagasta and Taltal regions, located within the Central Depression and the Domeyko Cordillera, display $\delta^{18}O_{SO4}$ and $\delta^{34}S_{SO4}$ values that imply a hydrothermal influence (Klipsch et al., 2023). However, their $^{87}Sr/^{86}Sr$ are around ~0.7070 and thus within the typical range of pedogenic Ca-sulfates, indicating that Ca—Sr and SO_4^{2-}anions have different sources.

In summary, we can therefore conclude that there is no specific hydrothermal Sr isotope signature in the region. Instead, the hydrothermal signature depends on that of the geological basement. Following this rationale, the water that fed the analyzed travertine is probably controlled by mafic or intermediate rocks with unradiogenic $^{87}Sr/^{86}Sr$, whereas the El Tatio hydrothermal water is buffered by more felsic units with radiogenic $^{87}Sr/^{86}Sr$ that underwent crustal contamination.

5.2.3. Andean basement and its interaction with meteoric water

An average Sr isotope signature of Andean weathering was previously proposed by Rech et al., 2003. These workers analyzed samples from salts and salar waters on the Altiplano in the Antofagasta region and calculated a mean $^{87}Sr/^{86}Sr$ value of ca. 0.70749. However, it is crucial to note that the regional Sr isotope signatures of Andean weathering can be expected to exhibit significant regional variability, mirroring the diverse lithologies of the Andean basement. Various studies have documented this radiogenic isotope variability, also providing a large dataset for different geological units within the Andes (e.g., Wörner et al., 1992; Lucassen et al., 1999; Kramer et al., 2005; Mamani et al., 2005). Across our study area (−19.4 to −25.0°S), the high Andes and the Precordillera span a $^{87}Sr/^{86}Sr$ range from ~0.7038 to ~0.7627 (Coira and Kay, 1993; Davidson and De Silva, 1995; De Silva et al., 1994; Feeley and Davidson, 1994; Francis et al., 1977; Godoy et al., 2018; Gonzales-Maurel et al., 2019; Hongda et al., 2019; Hawkesworth et al., 1982; Hawkesworth et al., 1979; Hilton et al., 1993; Kay et al., 1994; Meixner et al., 2020; Rabbia et al., 2017; Taussi et al., 2019; Thorpe et al., 1976; Wittenbrink, 1997). The majority of the data (~90 %) lie between ~0.7038 to ~0.7085, and the median of all data points is ~0.7067, slightly less radiogenic than the estimate by Rech et al., 2003.

The $^{87}Sr/^{86}Sr$ signature of the Central Andes and the Precordillera is transported into the Central Depression by groundwaters and rare surface water runoff. The $^{87}Sr/^{86}Sr$ values of groundwaters, salar waters and rivers within our dataset exhibit a narrow range (~0.7061 to ~0.7076). Our results are in line with the calculated median of the $^{87}Sr/^{86}Sr$ range given by the different Andean lithologies. The majority of water samples, however, show Sr isotope ratios higher than the median of 0.7067. Notable exceptions with $^{87}Sr/^{86}Sr < 0.7067$ include water samples taken from with the Tana/Tiliviche drainage, salar water from the Salar de Huasco, and groundwater samples from the Aguas Blancas region. The Tana / Tiliviche drainage water shows a $^{87}Sr/^{86}Sr$ ratio of 0.706373, and the corresponding suspended load an indistinguishable $^{87}Sr/^{86}Sr$ of 0.706351. Both of these unradiogenic Sr compositions may be attributed to the geologic units present in its catchment area. The source waters drain a Cenozoic volcanic shield (Fig. 6) with comparably unradiogenic $^{87}Sr/^{86}Sr$ (~0.7055; Wörner et al., 1992, De Silva et al., 1993 and Hoke and Lambs, 2007). Consequently, water-rock interaction between the Tana/Tiliviche drainage and this volcanic shield probably controls the system's budget. The Salar de Huasco, which is located at high altitudes (~3800 m) at around 20.3°S shows an even more unradiogenic Sr isotope composition of ~0.7062. The salar is mostly fed by the Collacagua river, which drains from north to south. In the north, this drainage system also taps the same unradiogenic volcanic shield as the Tana Tiliviche system (Fig. 6). The Aguas Blancas groundwater samples, located approx. 70 km southeast of Antofagasta, exhibit $^{87}Sr/^{86}Sr$ ratios of 0.7061 and 0.7065. According to Gamboa et al., 2019, groundwater in this region flows from the south / southeast toward north into the Aguas Blancas area. Their analysis of different groundwater samples taken in that area revealed a decreasing trend in $^{87}Sr/^{86}Sr$ ratios (from ~0.7073 to ~0.7070 to ~0.7068 to ~0.7069) with increasing latitude (from c. -24.6°S to c. -24.4°S), consistently with northward flow. The two Aguas Blancas samples (c. -24.1°S) presented here seem to represent the downstream end of this isotopic trend. As discussed above, this trend is probably caused by increasing water-rock interaction with less radiogenic geological units.

The observed uniform compositions of our water samples are in marked contrast to the large Sr isotope variability in the Andean basement rocks. Even more remarkable are the uniform $^{87}Sr/^{86}Sr$ patterns within the group of lacustrine salt samples (see Fig. 3). Both phenomena can be best explained by mixing and efficient pooling. Rivers and groundwater courses traverse various lithological units and integrate their Sr isotope budget. The actual impact of a lithological unit on the Sr signature of a water course is dependent on the specific rates of water-rock interaction during weathering or subsurface interaction, the Sr concentration within the rock units and the difference between the Sr isotope compositions of water and the bedrock.

Gamboa et al., 2019 analyzed the $^{87}Sr/^{86}Sr$ signature of different groundwater samples taken from the Atacama Desert. Although their study area (7500 km^2) is much smaller than the study area covered during this work (~200,000 km^2), there is a substantial variability among the $^{87}Sr/^{86}Sr$ of their groundwater samples. In contrast to our water samples, the water samples of Gamboa et al., 2019 were predominantly obtained from the Precordillera and the Altiplano at higher altitudes. Considering the typical water flow directions from the high Andes into the Central Depression, it is likely that the high-altitude water samples only had limited interactions with diverse lithological units. Consequently, their $^{87}Sr/^{86}Sr$ preserved more local and variable signatures. The findings of Gamboa et al., 2019 revealed that springs located below 3400 m display a relatively narrow range in $^{87}Sr/^{86}Sr$ from ~0.7073 to ~0.7078 and are frequently associated with Jurassic marine limestones (ranging from 0.7068 to 0.70785, Burke et al., 1982). In contrast, springs located above 3400 m exhibit a broader compositional range, reaching higher $^{87}Sr/^{86}Sr$ alues from ~0.7070 to ~0.7149. These springs are commonly linked to igneous Permian rocks, with $^{87}Sr/^{86}Sr$ values ranging from ~0.7078 to ~0.7173 (Gamboa et al., 2019).

Evaporites within the Central Depression are in most cases fed by watercourses and groundwater systems draining the Andes. Therefore, the precipitating salts will mirror the small variability in $^{87}Sr/^{86}Sr$ of these mixed water sources. Compared to the waters, however, the $^{87}Sr/^{86}Sr$ of evaporite salts including Ca-sulfate span an even smaller range (Fig. 3). This observation is best explained by additional mixing due to various erosion cycles and dissolution-reprecipitation, governed by wind and continuous groundwater flow. This is also supported by Jordan et al., 2022, who describe a repeated history of groundwater

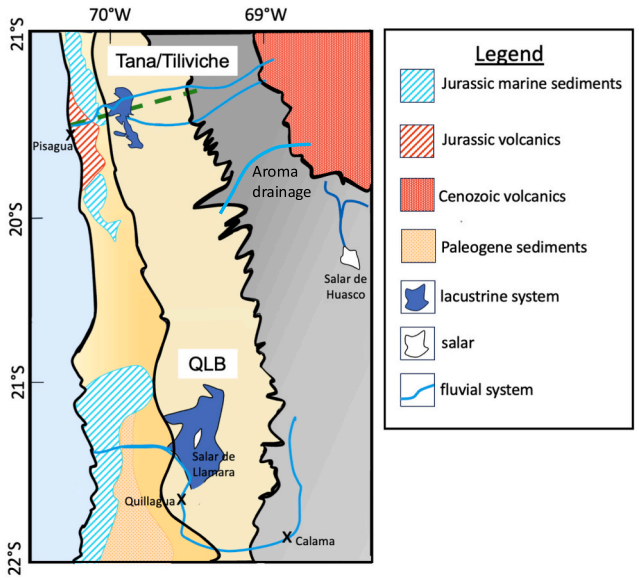

Fig. 6. Generalized geological map from 21°S to 22°S, illustrating the major basement units (Mapa Geologico de Chile, 2003) and the main hydrological features (Kirk-Lawlor et al., 2013; Ritter et al., 2018) as discussed in the text. Displayed lacustrine systems indicate former maximum extension. The dashed green line indicates the sampling transect for the Tiliviche area, see section 5.3.1. (For interpretation of the references to colour in this figure legend, the reader is referred to the web version of this article.)

exchange, further enhancing equilibration. In summary, we therefore cannot assign specific Sr isotope values to any endmembers discussed above, except the marine one (~0.7091) and a pooled composition of waters that have interacted with larger areas of basement (~0.7067).

5.3. Soil profiles

Pedogenic Ca-sulfate samples from soil profiles display a larger Sr isotope variability, than waters or lacustrine Ca-sulfates, indicating a higher variability of its Ca sources. This observation might be best explained by sampling local basement and not siliciclastics redistributed by aeolian processes, which are expected to homogenize the pedogenic Ca budget. However, groundwater processes that are shown above to homogenize lacustrine gypsum (section 5.2.3) may be a more effective way of homogenization. Additionally, as described in section 2.3, the majority of pedogenic samples analyzed here were selected to ensure that they were not influenced by surface water driven secondary redeposition (mixing) and were therefore located at local topographical heights. This sampling strategy again reduces the probability of external aeolian input.

We examined seven upper soil profiles from the Tiliviche area, Taltal, Mejillones, Tocopilla and the northern QLB. Within an idealized soil profile, the thenardites, analyzed along within some of these soil profiles, belong to the layer of highly soluble salts (Fig. 1). A notable feature of all soil profiles is that they are remarkably uniform in Sr isotope compositions along the individual depth profiles (Fig. 7). With the exception of two cases in the Tiliviche basin, different soil components exhibit nearly identical $^{87}Sr/^{86}Sr$ compositions. This was also shown by Consentino and Jordan, 2017 for 9 soil profiles.

In the Tiliviche soil profiles, different Sr isotope compositions are both displayed by siliciclastic components in the sulfates, and by the surface crusts. The different $^{87}Sr/^{86}Sr$ of the siliciclastic components probably reflect different transport mechanisms and limited exchange rates, as already discussed in section 5.1. Surface salts may accumulate through aeolian deposition and gradually exchange with underlying salts over time. At the Tiliviche site, the $^{87}Sr/^{86}Sr$ data show that isotopic equilibrium between surface and subsurface has not (yet) been fully established. This can be explained through different scenarios: (i) surface salts accumulate more rapidly compared to other sites, (ii) the exchange rates between surface and subsurface salts are particularly slow in this site, or (iii) the isotopic difference between the freshly accumulated surface salts and salts in the subsurface is larger.

The overall consistency of $^{87}Sr/^{86}Sr$ compositions within the diverse soil profiles is likely the product of efficient homogenization, governed by wind erosion, transport via groundwater and dissolution-reprecipitation processes. Thus, mixing also seems to operate also vertically. Infiltration of water, sourced by intermittent rain events or fog advection, dissolves and precipitates soil salts to a certain depth (see also Arens et al., 2021; Consentino and Jordan, 2017). In this perspective, utilizing the Sr isotope signatures across such depth profiles could potentially serve as an indicator for water infiltration depths and homogenization efficiency. Alternatively, the accumulated salts may originate from the same source at all times. In this regard, homogenous $^{87}Sr/^{86}Sr$ through a depth profile can also be interpreted as reflecting persistent environmental conditions, as previously discussed by Consentino and Jordan, 2017.

5.4. Sources and transport pathways within distinct basins

As outlined above, hydrologic transport pathways and endmember composition within the Atacama desert are complex. Therefore, two different basins, the Quillagua-Llamara and the Tiliviche basin, are discussed here in detail.

5.4.1. Tiliviche site

Based on sedimentological, stratigraphic and geomorphological evidence, Kirk-Lawlor et al., 2013 proposed the presence of a deep-water lake in the western Central Depression around 19.3 and 19.7°S near Pisagua during late Miocene to Pliocene (10.86 to 6.4 Ma). The Tiliviche lake was likely fed by the Tana/Tiliviche drainage, with possible contributions from the Aroma Drainage, as indicated by groundwater reservoirs in between (Fig. 6). Around 3.5 Ma ago, hydrological changes led to the termination of the lake stage, and the basin became drained by larger canyons. Subsequently, a groundwater-fed salar environment developed, leading to the accumulations of evaporites. The exact cause for termination of the salar system remains a topic of debate. Interpretations include tectonic factors (Binnie et al., 2020; Consentino and Jordan, 2017; Coudurier-Curveur et al., 2015; Evenstar et al., 2015; Garcia and Herail, 2005; Kirk-Lawlor et al., 2013) to climatic influences (Farías et al., 2005; Garcia et al., 2011; Jeffery et al., 2012).

In the Tiliviche basin, five water samples, three diatomite samples, six fossil salar Ca-sulfate samples, three siliciclastic samples and eight pedogenic samples were examined. Additionally, four data points provided in Consentino et al., 2015 who investigated pedogenic samples in this area were also included. The $^{87}Sr/^{86}Sr$ data analyzed for the Tiliviche area are shown in Fig. 8a. Two water samples originate from the Tana/Tiliviche drainage. Their $^{87}Sr/^{86}Sr$ isotope compositions are strongly similar, at ~0.7064, representing the lowest values within this dataset. In contrast, two water samples originating from the Aroma drainage display the highest $^{87}Sr/^{86}Sr$ ratios of water samples within the Tiliviche area at ~0.7075. The groundwater sample, taken between the Aroma drainage and the former Tiliviche lake, yields an intermediate value of ~0.7067 and the diatomites span an exceptional large range in $^{87}Sr/^{86}Sr$ compositions from ~0.7067 to ~0.7085. The upper value is the most radiogenic Sr composition measured inside this basin. The fossil salar Ca-sulfate samples exhibit $^{87}Sr/^{86}Sr$ ratios ranging from ~0.7065 to ~0.7071, falling within the range observed for the water samples. Notably, the pedogenic Ca-sulfate samples exhibit significantly more radiogenic values, ranging from ~0.7071 to ~0.7081.

For the Tiliviche basin, we analyzed two types of lacustrine sediments: diatomites and Ca-sulfates. The diatomites mirror the full lake stage before evaporite deposition and exhibit a large variety in

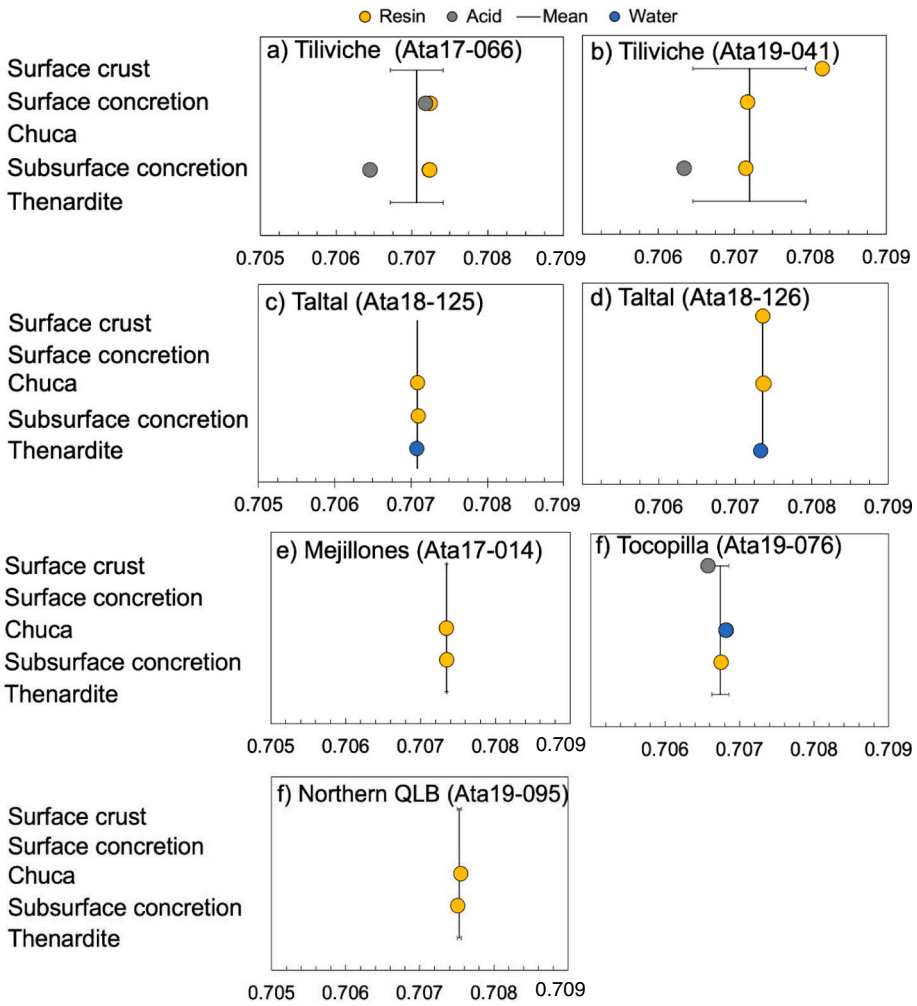

Fig. 7. $^{87}Sr/^{86}Sr$ compositions of different soil profiles. Symbol colors indicate the selective dissolution technique applied (see legend). See method section for details.

$^{87}Sr/^{86}Sr$. As discussed in section 5.2.3, a small variety in $^{87}Sr/^{86}Sr$ ratios is often attributed to a high degree of homogenization. On the contrary, the large variety in the Sr isotope composition of diatomites indicates more local signals. A highly radiogenic $^{87}Sr/^{86}Sr$ signal found for some of the diatomites may originate from the Costal Cordillera, which consists of Jurassic marine sediments and intrusive rocks of dacitic and andesitic composition (Mapa Geologico de Chile, 2003). Such material may have been transported in the Tiliviche basin through debris flows or surface water runoff along the eastern flank of the Coastal Cordillera.

The fossil salar Ca-sulfates within the Tiliviche lake exhibits more radiogenic $^{87}Sr/^{86}Sr$ than the present-day Tana/Tiliviche drainage. This difference may be explained either by (i) changes in the catchment area of the Tana/Tiliviche drainage, leading to interactions with different geological units, or (ii) by mixing with an additional source, shifting the $^{87}Sr/^{86}Sr$ composition of the entire water body to more radiogenic values. Kirk-Lawlor et al., 2013 proposed a hydrological connection between the former Tiliviche lake and the Aroma drainage in the south. Presently, the $^{87}Sr/^{86}Sr$ composition of the Aroma drainage is more radiogenic and thus, may constitute the additional source which contributed to the more radiogenic Sr budget of Tiliviche lake. Moreover, the $^{87}Sr/^{86}Sr$ composition of the groundwater, sampled between the former Tiliviche lake and the Aroma drainage, falls between the compositions of both river systems, further confirming a mixture of both water sources. However, it has to be noted, that the $^{87}Sr/^{86}Sr$ composition of the groundwater may have changed by recharge through the surrounding aquifer. The data presented here thus support the hypothesis of a hydrologic connection between the Aroma drainage and the ancient Tiliviche lake (cf. Kirk-Lawlor et al., 2013). The variations of Sr isotope compositions within the group of fossil salar Ca-sulfates may be explained by variable mixing ratios of Tana/Tiliviche and Aroma waters.

Pedogenic Ca-sulfates, in general, are supposed to be a secondary mixture of various sources, including marine sea spray, dust of lithologic origin and dust sourced by the weathering of primary salts (e.g., Arenas-Diaz et al., 2022; Ewing et al., 2006; Rech et al., 2003). Within the Tiliviche area, the analyzed (Holocene) pedogenic Ca-sulfates exhibit more radiogenic $^{87}Sr/^{86}Sr$ compared to corresponding water and lacustrine Ca-sulfates. This suggests the presence of an additional source with elevated $^{87}Sr/^{86}Sr$ ratios. A suitable radiogenic $^{87}Sr/^{86}Sr$ end-member in the Atacama Desert may be given by marine aerosols, delivering a $^{87}Sr/^{86}Sr$ ratio of ~0.7091 (Burke et al., 1982). However, in the Tiliviche basin, marine sea spray can be ruled out as a significant component for the Holocene to upper Pleistocene pedogenic samples. Such an influence of marine sea spray onto the pedogenic salt budget would be indicated by decreasing Sr isotope compositions with increasing coast distance (as already proposed by Rech et al., 2003) or, alternatively, decreasing Sr isotope compositions with increasing elevations outside of the marine fog zone (225–1075 m NN).

In Fig. 9, the $^{87}Sr/^{86}Sr$ compositions of the Tiliviche samples are displayed relative to coast distance and in relation to their elevation. As no variation between the $^{87}Sr/^{86}Sr$ of pedogenic Ca-sulfate with coastal

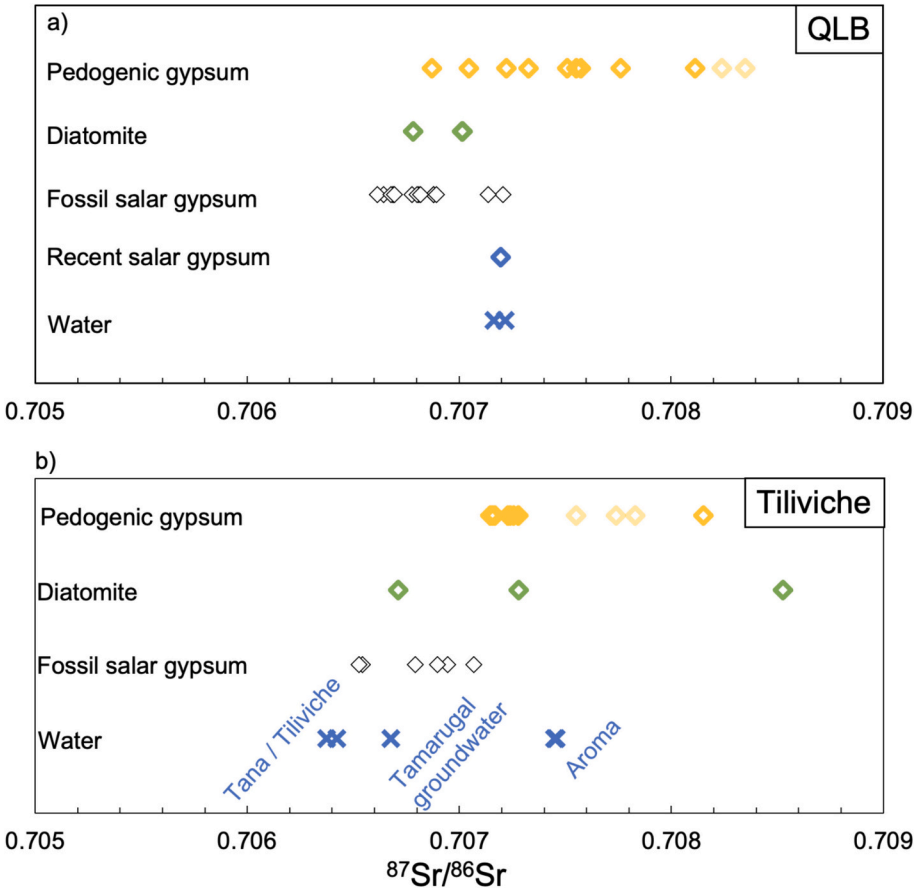

Fig. 8. Measured $^{87}Sr/^{86}Sr$ compositions of the different sample types within a) the Quillagua-Llamara basin and b) the Tiliviche basin. Pale symbols: Literature data from Consentino et al., 2015, who also analyzed Holocene Ca-sulfates samples.

distance or elevation (Fig. A3) is visible, marine aerosols are likely only a negligible constituent in the pedogenic salt budget of the Tiliviche area.

Consentino and Jordan, 2017 also investigated the Sr isotope composition of pedogenic Ca-sulfates from the Tiliviche area and evaluated the influence of marine sea spray on the salt budget. They came to the same conclusion that the pedogenic ion budget most probably did not receive significant marine contribution. However, their $^{87}Sr/^{86}Sr$ range (~0.7067 to ~0.7070) is lower than the data set reported here (~0.7065 to ~0.7078) and within the range of fossil lacustrine gypsum. Notably, the samples analyzed by Consentino and Jordan, 2017 are older (2.5 to 6.4 Ma).

A previously underestimated source of dust in the Tiliviche basin may be the Coastal Cordillera, from where weathered material may have been transported into the Central Depression by prevailing westerlies. The Coastal Cordillera in the Tiliviche area consists of granodiorites, diorites and granites dating back to the Jurassic to Cretaceous period (Mapa Geologico de Chile, 2003). These rocks are enriched in incompatible elements and thus, likely have developed radiogenic $^{87}Sr/^{86}Sr$ over time. Wang et al., 2014 analyzed such wind-transported dust material, transported from the Coastal Cordillera in to the Central Depression by using dust traps, installed east from Mejillones peninsula. The main portion of this dust consists of insoluble materials, i.e. siliciclastic particles, supporting the hypothesize that siliciclastic dust with radiogenic $^{87}Sr/^{86}Sr$ contributes to the pedogenic salt budget within the Central Depression. Nevertheless, it cannot be excluded that gypsum soil from the Coastal Cordillera also contributes to the Ca—Sr budget. In contrast, winds transporting sediment from the east are not likely to raise the $^{87}Sr/^{86}Sr$ ratio. During the Austral summer, easterly winds above the Andes occur due to the southward shift of the Bolivian high (Reyers et al., 2019). Nevertheless, in the specific latitudinal range in the high Andes (19.15–19.60°S), only young volcanic rocks of Neogene to upper Paleogene age are exposed, displaying more unradiogenic $^{87}Sr/^{86}Sr$. Hence, it is unlikely that material from these rocks significantly raised the Sr compositions of the pedogenic salts.

Within the Tiliviche basin, three pedogenic Ca-sulfate samples were additionally analyzed for their inherent siliciclastic components, (see method section above and Fig. A2). Notably, the $^{87}Sr/^{86}Sr$ of the siliciclastic components are significantly less radiogenic than those of their ambient Ca-sulfate hosts. Consequently, it is evident that the radiogenic Sr isotope compositions of these three pedogenic samples cannot be equilibrated with the siliciclastic grains.

Another potential source of high radiogenic Sr may be represented by the Jurassic marine limestones that occur in the Coastal Cordillera (Mapa Geologico de Chile, 2003). Unfortunately, no $^{87}Sr/^{86}Sr$ data for this geologic unit are currently available. However, as marine limestones inherit their Sr isotopic signature from the ambient ocean water at the time of their deposition, the global marine Sr curve allows an estimation of the Sr composition of these rocks. According to McArthur et al., 2020, the Sr isotope composition during the Jurassic varies between 0.7068 and 0.7077, with an average value of 0.7072. Whilst this range is rather unradiogenic, it is still higher than that of the pedogenic samples. Wang et al., 2014 did not identify significant amounts of carbonate within their aolian dust traps. Though, a significant aeolian transport of Jurassic marine limestones (i.e. carbonate) into the Central Depression is not very plausible. Alternatively, dissolved limestones may be transported by groundwater flow from the Coastal Cordillera into the Central Depression. Herrera et al., 2018 analyzed the $^{87}Sr/^{86}Sr$ of groundwater samples taken from the Coastal Cordillera. Groundwater samples taken from coastal springs vary between 0.70635 and 0.70867,

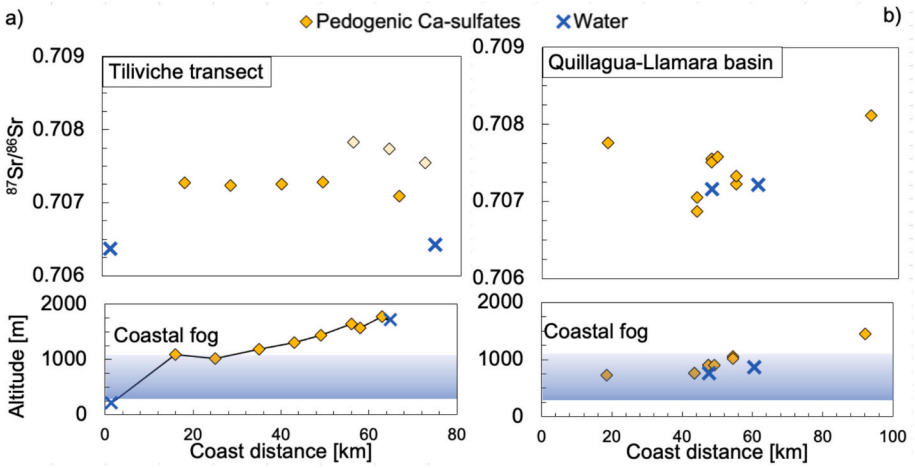

Fig. 9. Variation of Sr isotope compositions (upper panel) and altitude (lower panel) versus coastal distance for the Tiliviche transect (a)) and for the QLB (b). Displayed Tiliviche samples are those located close to the red transect line in Fig. 6. Pale coloured symbols: Literature data from Consentino et al., 2015, who also analyzed Holocene Ca-sulfate samples. (For interpretation of the references to colour in this figure legend, the reader is referred to the web version of this article.)

showing a large overlap with Jurassic marine ocean water, making groundwater flow a plausible pathway. Consentino and Jordan (2017) measured less radiogenic $^{87}Sr/^{86}Sr$ ratios in pedogenic Ca-sulfates from Miocene to Pliocene age in the Tiliviche area. This may imply that transport of radiogenic Sr into the Central Depression was less active or not active during Miocene to Pliocene times.

5.4.2. *Quillagua-Llamara basin*

The Quillagua-Llamara-Basin (QLB) represents a former lake system once fed by the Rio Loa river. This drainage system originates in the high Andes, also drains the Calama basin and was also fed by ephemeral creeks from the Precordillera. The transformation of this lacustrine system from endorheic to exorheic occurred due to the incision of the Rio Loa canyon, leading to the successive decrease of the water table and evaporite deposition. Evidence of this former lake system is given by thick layers of lake deposits and evaporites within the Quillagua and Soledad formations. The Salar de Llamara represents a remnant of this paleo-lake system and is fed by a northern groundwater flow (Jordan et al., 2018; Jordan et al., 2022; Ritter et al., 2018; Sáez et al., 1999). During times of rare but extreme rain events, the salar system is also fed by surface water flow (Olivares and Jordan, 2024).

The $^{87}Sr/^{86}Sr$ data for QLB samples are displayed in Fig. 8a. Two water samples were also examined, of which one was taken at the estuary of the Rio Loa and a second from the groundwater flowing into the Salar de Llamara. Their $^{87}Sr/^{86}Sr$ are very similar (~0.70722 and ~ 0.70716, respectively). The recent salar Ca-sulfate from the Salar de Llamara (Ata17–130) exhibits a virtually identical $^{87}Sr/^{86}Sr$ of 0.707196. The $^{87}Sr/^{86}Sr$ of the fossil lacustrine Ca-sulfates, obtained from the Quillagua and Soledad formation, span a range from ~0.7066 to ~0.7072. The diatomite samples, which underlie the lacustrine gypsum, exhibit $^{87}Sr/^{86}Sr$ between ~0.7068 to ~0.7070. The pedogenic samples, while partially overlapping with the waters and some of the fossil salar Ca-sulfate samples, extend to significant more radiogenic values, reaching up ~0.7084. The similar $^{87}Sr/^{86}Sr$ of the diatomites and fossil Ca-sulfates indicate a comparable water source for both the lake and the salar stages. Conversely, the present-day water sources (Rio Loa and groundwater) exhibit significantly more radiogenic $^{87}Sr/^{86}Sr$ than the fossil lacustrine sediments. In analogy to the Tiliviche basin (Fig. 9), this suggests a shifted drainage area of the Rio Loa River or the presence of an additional source contributing to the lake system. The latter possibility may be supported by the ephemeral creeks draining from the Precordillera.

Jordan et al., 2022 studied the evolution of the Quillagua depocenter between 9 and 2.6 Ma. According to their work, the Quillagua formation accumulated in a relatively wet period, where a constant surface water flow was supplied by the paleo-Loa river. Additionally, the ephemeral creeks in the Precordillera which interacted with a freshly deposited ingnimbrite ('Carcote' ignimbrite, Ancachi formation, 5.8 Ma) played an important role. During the deposition of the Soledad formation, the climate was drier and the Quillagua lake turned into a salar environment fed by groundwater from the Calama basin and ephemeral streams from the Precordillera. The 'Carcote' ignimnrite was probably completely eroded during that time.

Our work does not rule out the possibility of a changed drainage area of the Rio Loa, but supports the hypothesis of Jordan et al., 2022, that the Precordillera influences the ion budget inside the Quillagua depocenter.

The pedogenic samples of the QLB exhibit elevated $^{87}Sr/^{86}Sr$ in comparison to other sample types, suggesting an additional source contributing to the pedogenic salt budget. Within the latitudinal range of the QLB, the Coastal Cordillera is comparably low with several corridors that would allow fog to penetrate. Therefore, marine fog may represent a potential radiogenic source of salts. However, there is no clear correlation between $^{87}Sr/^{86}Sr$ ratios and altitude (Fig. A3). Since the sample locations are not aligned along a single transect but are rather distributed across the region, this pattern may rather reflect localized influences than a consistent altitudinal trend.

As for the Tiliviche basin, radiogenic Sr might also be delivered by erosion of Jurassic marine limestones. Within the QLB latitude, this unit is present in the Coastal Cordillera as well as in the Cerro Soledad (Vásquez et al., 2018).

The observations suggest that both marine fog and erosion of radiogenic lithologies, such as Jurassic marine limestones, may play a role in the enriched Sr composition of the pedogenic samples inside the QLB.

5.5. *A model for Sr sources and transport processes within the Atacama Desert*

By combining our $^{87}Sr/^{86}Sr$ data with findings from literature using sulfate isotopes (Bao et al., 2004; Klipsch et al., 2023; Michalski et al., 2004; Rech et al., 2003), it is now possible to develop a comprehensive model for the sources and transport processes contributing to the elemental Ca-sulfate budget within the Atacama Desert, illustrated in Fig. 10. The data demonstrate that Ca and S are delivered by different sources. The sulfur budget is primarily dominated by SAS of atmospheric and marine origin, along with biologically recycled sulfur (cf. Klipsch et al., 2023). The amount of marine PAS and SAS decrease with

increasing coast distance (Fig. 10, arrow 2), while atmospheric SAS of anthropogenic and volcanic origin is deposited evenly across the whole Atacama Desert (arrow 3). Biologic sulfur cycling takes place in playa like environments under water availability (arrow 7). The amount of sulfur, sourced by the Andes (arrows 9 and 10), is difficult to quantify as it does not carry a distinct S isotope signature (Klipsch et al., 2023).

In contrast to S, the Ca budget is mainly sourced from rock weathering in the high Andes and the Coastal Cordillera (arrow 4, 9 and 10). Additionally, at altitudes below 1075 m, marine Ca is also stored within the salt deposits in significant amounts (arrow 2). Other important processes, responsible for the homogeneous Sr isotopic signal across the Atacama Desert, are lateral and vertical homogenization processes (arrow 5 and 8) as described in section 5.2.4.

6. Conclusions

Our study presents a comprehensive model for the sources of Ca in Ca-sulfates of the Atacama Desert using Sr isotopes. We present a novel selective digestion method for impure Ca-sulfate samples and apply this protocol to a representative set of evaporite samples, their siliciclastic components and a corresponding set of water samples from the Atacama Desert in Chile. Several key findings can be inferred:

1. The selective digestion method using anion resin is suitable for analyzing Sr isotope compositions in evaporate samples with mixed mineralogy. Within a single sample, highly water-soluble salts are frequently in equilibrium with Ca sulfates due to their common origin and rapid equilibration rates. In contrast, siliciclastics are usually not in equilibrium due to differences in their transport mechanisms and slow exchange rates in water-limited environments.
2. Andean basement rocks constitute a significant source to the Ca budget of the Atacama evaporites. The $^{87}Sr/^{86}Sr$ range of the Andean siliciclastics exhibit a great range. However, the Sr budget within the Atacama Desert salts is notably homogenous due to complex pooling and mixing cycles both laterally and vertically. We infer a typical value of ~0.7067 for salt-forming brines. This efficient pooling and mixing process operates through erosion and dissolution-reprecipitation reactions and is also driven by wind, groundwater flow and fog infiltration.
3. Soil salts often show more radiogenic $^{87}Sr/^{86}Sr$ compared to waters and lacustrine Ca-sulfate. While marine fog may contribute to the pedogenic salt budget in low areas within the Coastal Cordillera, for example in the QLB, the absence of correlation of $^{87}Sr/^{86}Sr$ with coastal distance or altitude indicates an additional high $^{87}Sr/^{86}Sr$ source other than sea spray. The radiogenic Sr may be supplied by Sr-rich, weathered Jurassic carbonate rocks from the Coastal Cordillera.
4. The Sr isotope data allow further inferences on paleo-drainage patterns. $^{87}Sr/^{86}Sr$ compositions of fossil salar Ca-sulfate from the former Tiliviche lake at ca. -19.5°S, in comparison to that of the recent inflowing water, suggests a past hydrologic connection to the Aroma drainage in the south. This confirms a previous model by Kirk-Lawlor et al., 2013.
5. The combination of the $^{87}Sr/^{86}Sr$ data gained within this study with previous sulfur and Sr isotope data from literature allows further insights into the important Ca sources and ion fluxes operating within the Atacama Desert, responsible for the extensive Ca-sulfate

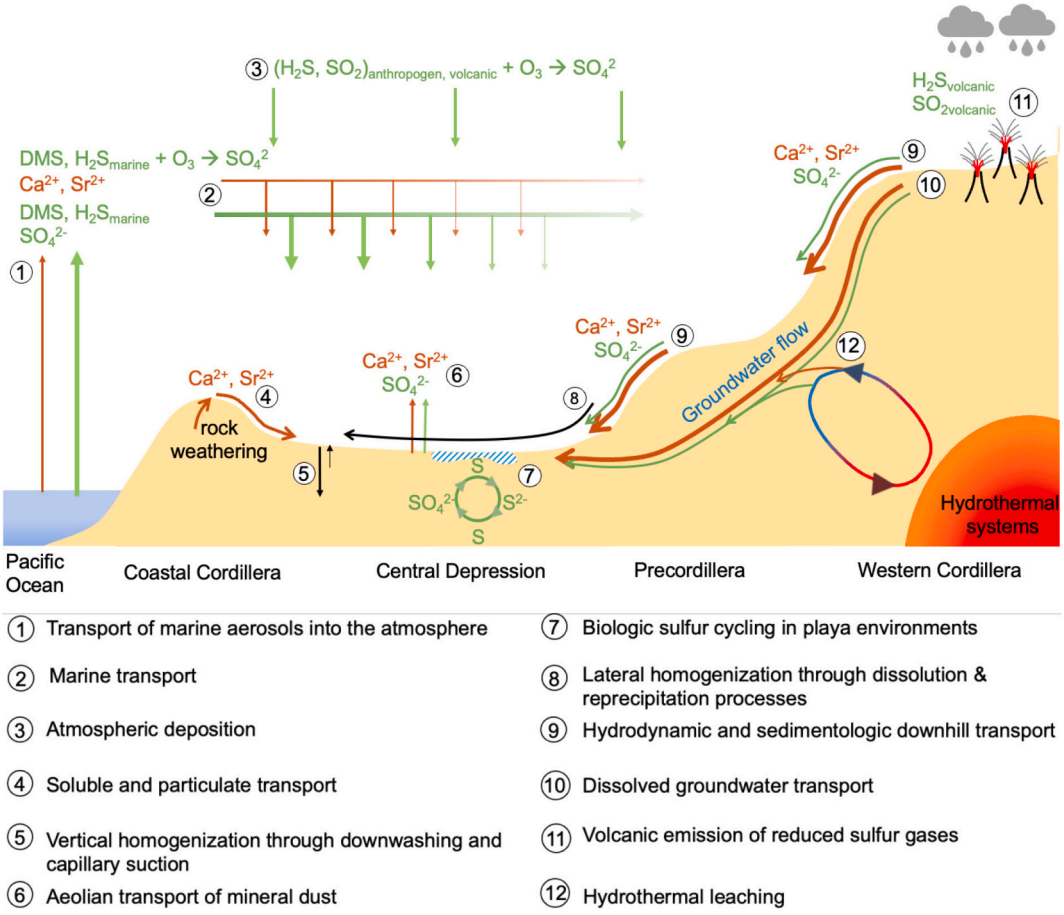

Fig. 10. Schematic cross section through the Atacama Desert, illustrating the main ion sources and fluxes relevant for Ca-sulfate deposition. Green arrows indicating sulfur fluxes, brownish arrows Ca^{2+} fluxes. (For interpretation of the references to colour in this figure legend, the reader is referred to the web version of this article.)

deposits. While sulfur is mainly sourced by the ocean and the atmosphere, Ca is mainly sourced by rock weathering.

CRediT authorship contribution statement

Katharina Deußen: Writing – original draft, Visualization, Methodology, Formal analysis, Data curation. **Carsten Münker:** Writing – review & editing, Validation, Supervision, Resources, Project administration, Investigation, Funding acquisition, Conceptualization. **Michael Staubwasser:** Resources, Project administration, Methodology, Investigation, Conceptualization.

Declaration of generative AI and AI-assisted technologies in the writing process

During the preparation of this work the author(s) used ChatGPT (OpenAI) in order to improve the language of that manuscript. After using this tool/service, the author(s) reviewed and edited the content as needed and take(s) full responsibility for the content of the publication.

Declaration of competing interest

The authors declare that they have no known competing financial interests or personal relationships that could have appeared to influence the work reported in this paper.

Acknowledgements

This project was founded by DFG CRC1211, project C04.

We want to thank F. Wombacher and A. Katzemich for their valuable support during sample preparation and analysis. We thank B. Ritter for helpful discussions.

We are also greatful to T. Jordan for her constructive feedback and in-depth knowledge of the Atacama Desert during the review process of that manuscript. Editorial handling by Dr. C. Romano is also acknowledged.

We want to thank C. Romano for the review of this article.

Appendix A. Supplementary data

Supplementary data to this article can be found online at https://doi.org/10.1016/j.chemgeo.2025.122956.

Data availability

Data will be made available on request.

References

Allmendinger, R.W., Gonzales, G., 2010. Invited review paper. Neogene to Quaternary tectonics of the coastal Cordillera, northern Chile. Tectonophysics 495 (1-2), 93–110.

Arenas-Diaz, F., Fuentes, B., Reyers, M., Fiedler, S., Böhm, C., Campos, E., Shao, Y., Bol, R., 2022. Dust and aerosols in the Atacama Desert. Earth Sci. Rev. 226.

Arens, F.L., Ario, A., Feige, J., Sager, C., Wiechert, U., Schulze-Makuch, D., 2021. Geochemical proxies for water-soil interactions in the hyperarid Atacama Desert, Chile. CATENA 206.

Bao, H., Jenkins, K.A., Khachaturyan, M., Diaz, G.C., 2004. Different sulfate sources and their post-depositional migration in Atacama soils. Earth Planet. Sci. Lett. 224, 557–587.

Berger, I.A., Cooke, R.U., 1997. The origin and distribution of salts on alluvial fans in the Atacama Desert, northern Chile. Earth Surf. Proc. Land 22, 581–600.

Binnie, S.A., Reicherter, K.W., Victor, P., Gonzalez, G., Binnie, A., Niemann, K., Stuart, F. M., Lenting, C., Heinze, S., Freeman, S.P.H.T., Dunai, T.J., 2020. The origins and implications of paleochannels in hyperarid, tectonically active regions. The northern Atacama Desert, Chile. Glob. Planet. Change 185, 103083.

Böhlke, J.K., Ericksen, G.E., Revesz, K., 1997. Stable isotope evidence for an atmospheric origin of desert nitrate deposits in northern Chile and southern California, U.S.A. Chem. Geol. 136, 135–152.

Brimblecombe, 2013. The Global Sulfur Cycle, 2 ed. 10. Elsevier Ltd.

Burke, W.H., Denison, R.E., Hetherington, E.A., Koepnik, R.B., Nelson, H.F., Otto, J.B., 1982. Variation of seawater $^{87}Sr/^{86}Sr$ throughout Phanerozoic time. Geology 10, 516–519.

Chong, G., 1988. The Cenozoic saline deposits of the Chilean Andes between 18° and 27° south. In: Baghlburg, H., Breitkreuz, C., Giese, P. (Eds.), The southern Central Andes. Springer-Verlag, pp. 135–151.

Claridge, G.G.C., Campbell, I.B., 1968. Origin of nitrate deposits. Nature 217, 428–430.

Coira, B.L., Kay, S.M., 1993. Implications of quaternary volcanism at Cerro Tuzgle for crustal and mantle evolution of the Puna Plateau, Central Andes, Argentina. Contrib. Mineral. Petrol. 113, 40–58.

Coira, B., Davidson, J., Mpodozis, C., Ramos, V., 1982. Tectonic and magmatic evolution of the Andes of Northern Argentina and Chile. Earth Sci. Rev. 18, 303–332.

Consentino, N.J., Jordan, T.E., 2017. 87Sr/86Sr of calcium sulfate in ancient soils of hyperarid settings as paleoaltitude proxy. Pliocene to Quaternary constraints for northern Chile (19.5 – 21.7°S). Tectonics 36, 137–162.

Consentino, N.J., Jordan, T.E., Derry, L.A., Morgan, J.P., 2015. 87Sr/86Sr in recent accumulations of calcium sulfate on landscapes of hyperarid settings: a bimodal altitudinal dependence for northern Chile (19.5-21.5°S). Geophys. Geochem. Geosyst. 16, 4311–4328.

Cortecci, G., Boschetti, T., Mussi, M., Herrera Lameli, C., Muccino, C., Barbieri, M., 2005. New chemical and original isotopic data on waters from El Tatio geothermal field, northern Chile. Geochem. J. 39, 547–571.

Cortés, C., JoaquínMarquardt, R., Carlos, González L., Gabriel, Wilke H., Hans, G., Marinovic, S., Nicolás, 2007. Región de Antofagasta Escala 1:100.000.

Coudurier-Curveur, A., Lacassin, R., Armijo, R., 2015. Andean growth and monsoon winds drive landscape evolution at SW margin of South America. Earth Planet. Sci. Lett. 414, 87–99.

Davidson, J.P., De Silva, S.L., 1995. Late cenozoic magmatism of the Bolivian Altiplano. Contrib. Mineral. Petrol. 119, 387–408.

De Silva, S.L., Davidson, J.P., Croudace, I.W., Escobar, A., 1993. Volcanological and petrological evolution of volcan Tata Sabaya, SW Bolivia. Volcanol. Geotherm. Res. 55, 305–335.

De Silva, S.L., Self, S., Francis, P.W., Drake, R.E., Ramirez, R.C., 1994. Effusive silicic volcanism in the Central Andes. The Chao Dacite and other young lavas of the Altiplano-Puna Volcanic complex. J. Geophys. Res. B99, 17805–17825.

Del Rio, C., Garcia, J.-L., Osses, P., Zanetta, N., Lambert, F., Rivera, D., Siegmund, A., Wolf, N., Cereceda, P., Larrain, H., Lobos, F., 2018. ENSO influence on Coastal Fog-Water Yield in the Atacama Desert, Chile. Aerosol Air Qual. Res. 18, 127–144. https://doi.org/10.4209/aaqr.2017.01.0022.

Del Rio, C., Lobos-Roco, F., Latorre, C., Koch, M.A., Garcia, J.-L., Osses, P., Lambert, F., Alfaro, F., Siegmund, A., 2021. Spatial distribution and interannual variability of coastal fog and low clouds cover in the hyperarid Atacama Desert and implications for past and present Tillandsia landbeckii ecosystems. Plant Syst. Evol. 307, 58.

Denison, R.E., Kirkland, D.W., Evans, R., 1998. Using Sr isotopes t odetermine the Age and Origin of Ca-sulfate and Anyhdrite Beds. J. Geol. 106 (1), 1–18.

DGA, 1987. Balance hidrico de Chile. Ministerio de Obras Publicas, Santiogao, Chile, Direccion General de Aguas.

Di Celma, C., Pierantoni, P.P., Cantalamessa, G., 2014. Geological map of the Miocene – Pleistocene successions of the Mejillones Peninsula, Northern Chila. J. Maps 10, 350–363.

Ericksen, 1961. Rhyolite tuff, a source of the salts of northern Chile. In: USGS Professional Paper, 424-C, pp. 224–225.

Ericksen, G.E., 1981. Geology and Origin of the Chilean Nitrate Deposits. USGS, Washington, p. 37 (Report No. 1188).

Ericksen, G.E., 1983. The Chilean Nitrate Deposits. Am. Sci. 71, 366–374.

Evenstar, L.A., Mather, A.E., Hartley, A.J., Tattitch, B., 2015. Slow Cenozoic uplift of the western Andean Cordillera indicated by cosmogenic ^{3}He in alluvial boulderns from the Pacific Planation Surface. Geophys. Res. Lett. 42, 1–8.

Ewing, S.A., Sutter, B., Owen, J., Nishiizumi, K., Sharp, W., Cliff, S.S., Perry, K., Dietrich, W., McKay, C.P., Amundson, R., 2006. A threshold in soil formation at Earth's arid-hyperarid transition. Geochim. Cosmochim. Acta 70, 5293–5322.

Farías, M., Charrier, R., Comte, D., Martinod, J., Hérail, G., 2005. Late Cenozoic deformation and uplift of the western flank of the Altiplano. Evidence from the depositional, tectonic, and geomorphologic evolution and shallow seismic activity (northern Chile at 19°30′S). Tectonics 24, 1–27.

Feeley, T.C., Davidson, J.P., 1994. Petrology of calc-alkaline lavas of volcan n ollagüe and the origin of compositional diversity at central Andean stratovolcanoes. J. Petrol 35, 1295–1340.

Francis, P.W., Moorbath, S., Thorpe, R.S., 1977. Strontium isotope data for recent andesites in Ecuador and North Chile. Earth Planet. Sci. Lett. 37, 197–202.

Gamboa, C., Godfrey, L., Herrera, C., Custodio, E., Soler, A., 2019. The origin of solutes in groundwater in a hyper-arid environment. A chemical and multi-isotope approach in the Atacama Desert, Chile. Sci. Total Environ. 690, 329–351.

Garcia, M., Herail, G., 2005. Fault-related folding, drainage network evolution and valley incision during the Neogene in the Andean Precordillera of Northern Chile. Geomorphology 65, 279–300.

Garcia, M., Riquelme, R., Farias, M., Herail, G., Charrier, R., 2011. Late Miocene-Holocene canyon incision in the western Altiplano, northern Chile. Tectonic or climatic forcing? J. Geol. Soc. London 168, 1047–1060.

Garreaud, R., Christie, D., Barichivih, J., Maldonado, A., 2007. Climate, weather and fog along the west coast of Suptropical South America. In: 4th International Conference on Fog, Fog Collection and Dew, Proceedings, La Serena, Chile, 2007, pp. 22–27.

Giggenbach, W.F., 1978. The isotope composition of waters from the El Tatio geothermal field, Nothern Chile. Geochim. Cosmochim. Acta 42 (7), 979–988.

Godoy, B., Lazcano, J., Rodriguez, I., Martinez, P., Parada, M.A., Le Roux, P.J., Wilke, H. G., Polanco, E., 2018. Geological evolution of Paniri Volcano, Central Andes, Northern Chile. J. S. Am. Earth Sci. 84, 184–200.
Gonzales-Maurel, O., Le Roux, P.J., Godoy, B., Troll, V.R., Deegan, F.M., Menzies, A., 2019. The great escape. Petrogenesis of low-silica volcanism of Pliocene to Quaternary age associated with the Altiplano-Puna volcanic compley of Northern Chile (21°10′ – 22°50'S). Lithos 346–347.
Hartley, A.J., Evenstar, L., 2010. Cenozoic stratigraphic development in the north Chilean forearc. Implications for basin development and uplift history of the Central Andean margin. Tectonophysics 495 (1–2), 67–77.
Hartley, A.J., May, G., Chong, G., Turner, P., Kape, S.J., Jolley, E.J., 2000. Development of a continental forearc. A Cenozoic example from the Central Andes, northern Chile. Geology 28 (4), 331–334.
Hawkesworth, C.J., Norry, M.J., Roddick, J.C., Baker, P.E., Francis, P.W., Thorpe, R.S., 1979. 143Nd/144Nd, 87Sr/86Sr and incompatible element variations in calc-alkaline and plateau lavas from South America. Earth Planet. Sci. Lett. 42, 45–57.
Hawkesworth, C.J., Hammill, M., Gledhill, A.R., Van Calsteren, P.W., Rogers, G., 1982. Isotope and trace element evidence for late-stage intra-crustal melting in the High Andes. Earth Planet. Sci. Lett. 58, 240–254.
Herrera, C., Gamboa, C., Custodio, E., Jordan, T., Godfrey, L., Jodar, J., Luque, J.A., Vargas, J., Saez, A., 2018. Groundwater origin and recharge in the hyperaric Cordillera de la Costa, Atacama Desert, northern Chile. Sci. Total Environ. 624, 114–132.
Hilton, D.R., Hammerschmidt, K., Teufel, S., Friedrichsen, H., 1993. Helium isotope characteristics of Andean Geothermal fluids and lavas. Earth Planet. Sci. Lett. 120, 265–282.
Hoke, L., Lambs, S., 2007. Cenozoic behind-arc volcanism in the Bolivian Andes, South America. Implications for mantle melt generation and lithosphere structure. J. Geol. Soc. London 164, 795–814.
Hongda, Hao, Campbell, I.H., Richards, J.P., Nakamura, E., Sakaguchi, C., 2019. Platinum-group element geochemistry of the Escondida Igneous Suites, Northern Chile. Implications for ore formation. J. Petrol. 60.
Houston, J., Hartley, A.J., 2003. The central Andean west-slope rainshadow and its potential contribution to the origin of hyper-aridity in the Atacama Desert. Int. J. Climatol. 23, 1453–1464.
Jeffery, L.M., Poulsen, C.J., Ehlers, T.A., 2012. Impacts of Cenozoic global cooling, surface uplift, and an inland seaway on south American paleoclimate and precipitation $\delta^{18}O$. Bull. Geol. Soc. Am. 124, 335–351.
Jordan, T.E., Kirk-Lawlor, N.E., Blanco, N.P., Rech, J.A., Cosentino, N.J., 2014. Landscape modification in response to repeated onset of hyperarid paleoclimate states since 14 Ma, Atacama Desert, Chile. Geol. Soc. Am. Bull. 126, 1016–1046.
Jordan, T.E., Blanco, N., Quezada, A., Jensen, A., Vásquez, P., Sepúlveda, F., 2018. Comment on paper by Ritter et al. (2018) Evidence for multiple Plio-Pleistocene lake episodes in the hyperarid Atacama Desert. Quat. Geochronol. 44, 1–12.
Jordan, T.E., Quezada, A., Blanco, N., Jensen, A., Vásquez, P., Supulveda, F., 2022. Paleoenvironmental evolution of a forearc in response to forcings by drainage, climate, volcanism, and tectonics. The Quillagua Depocenter, Chile. Lithosphere2022 1, 1024844.
Karatson, D., Telbisz, T., Wörner, G., 2012. Erosion rates and erosion patterns of Neogene to Quaternary stratovolcanoes in the Western Cordillera of the Central Andes. An SRTM DEM based analysis. Geomorphology 139-140, 122–135.
Kay, S.M., Coira, B.L., Viramonte, J.M., 1994. Young Mafic Back Arc volcanic rocks as indicators of continental lithospheric delamination beneath the argentine Puna Plateau, Central Andes. J. Geophys. Res. B99, 24323–24339.
Kirk-Lawlor, N.E., Jordan, T.E., Rech, J.A., Lehmann, S.B., 2013. Late Miocene to early Pliocene paleohydrology and landscape evolution of Northern Chile, 19° to 20°S. Paleogeogr. Palaeoclimatol. Palaeoecol. 387, 76–90.
Klipsch, S., Herwartz, D., Voigt, C., Münker, C., Chong, G., Böttcher, M., Staubwasser, M., 2023. Sulfate sources, biologic cycling and mobility in Atacama Desert soils revealed by isotope signatures. Global Planet.Change 230.
Kramer, W., Siebel, W., Romer, R.L., Haase, G., Zimmer, M., Ehrlichmann, R., 2005. Geochemical and isotopic characteristics and evolution of the Jurassic volcanic arc between Arica (18.5°S) and Tocopilla (22°S), north Chilean Coastal Cordillera. Geochemistry 65. https://doi.org/10.1016/j.chemer.2004.01.002.
Leybourne, M.I., Cameron, E.M., Reich, M., Palacios, C., Faure, K., Johannesson, K.H., 2013. Stable isotope composition of soil calcite (O. C) and Ca-sulfate (S) overlying Cu deposits in the Atacama Desert, Chile. Implications for mineral exploration, salt sources and paleoenvironmental reconstruction. Appl. Geochem. 29, 55–72.
Lucassen, F., Franz, G., Thirlwall, M.F., Mezger, K., 1999. Crustal recycling of metamorphic basement. Late Paleozoic granitoids of northern Chile (about 22°S). Implications for the composition of the Andean crust. Petrol 40, 1527–1551. https://doi.org/10.1093/petroj/40.10.1527.
Mamani, M., Tassara, A., Wörner, G., 2005. Composition and structural control of crustal domains in the Central Andes. Geochem. Geophys. Geosyst. 9. https://doi.org/10.1029/2007GC001925.
Mapa Geologico de Chile, 2003. Publication Geologica Digital, No. 4. Servicio Nacional de Geologia y Mineria.
McArthur, J.M., Howarth, R.J., Shields, G.A., Zhou, Y., 2020. Strontium isotope stratigraphy, Chapter 7, p211 – p238. In: Gradstein, F.M., Ogg, J.G., Schmitz, M.D., Ogg, G.M. (Eds.), A Geologic Time Scale. Elsevier B.V., 1 of 2, p. 1357.
Meixner, A., Sarchi, C., Lucassen, F., Becchio, R.A., Caffe, P.J., Lindsay, J.M., Rosner, M., Kasemann, S.A., 2020. Lithium concentrations and isotope signatures of palaeozoic basement rocks and cenozoic volcanic rocks from the Central Andean Arc and Back-Arc. Miner. Depos. 55, 1071–1084.
Michalski, G., Böhlke, J.K., Thiemens, M., 2004. Long term atmospheric deposition as the source of nitrate and other salts in the Atacama Desert, Chile. New evidence from mass-independent oxygen isotope compositions. Geochim. Cosmochim. Acta 68, 4023–4038.
Müller, D.W., Mueller, P.A., 1991. Origin and age oft he Mediterranean Messinian evaporites. Implications from Sr isotopes. Earth Planet. Sci. Lett. 107 (1), 1–12.
Münker, C., Bartolome, M., Obert, C., Staubwasser, M., 2023. Dating of Ca-sulfate from different depositional environments using U-Pb and U-series geochronology. In: Goldschidt Conference, Lyon.
Olivares, L., Jordan, T.E., 2024. Contributions by extreme rain events to long-term hyperarid landscape evolution. Quat. Sci. Rev. 332, 10.
Pérez-Fodich, A., Reich, M., Alvarez, F., Snyder, G.T., Schoenberg, R., Vargas, G., Muramatsu, Y., Fehn, U., 2014. Climate change and tectonic uplift triggered the formation of the Atacama Desert's giant nitrate deposits. Geology 42 (3), 251–254.
Rabbia, O.M., Correa, K.J., Hernandez, L.B., Ulrich, T., 2017. "Normal" to adakite-like arc magmatism associated with the el abra porphyry copper deposit, Central Andes, Northern Chile. Int. J. Earth Sci. 106, 2687–2711.
Ramos, V.A., 2009. The tectonic regime laong the Andes. Present-day and Mesozoic regimes. Geol. J. 45, 2–25.
Rech, J.A., Quade, J., Hart, W.S., 2003. Isotopic evidence fort he source of ca and S in soil Ca-sulfate, anhydrite and calcit3e in the Atacama Desert, Chile. Geochim. Cosmochim. Acta 67 (4), 575–586.
Reyers, M., Reyers, M., Hamidi, M., Shao, Y., 2019. Synoptic analysis and simulation of an unusual dust event over the Atacama Desert. Atmos. Sci. Lett. 20, 1–9.
Risacher, F., Fritz, B., 2009. Origin of Salts and Brine Evolution of Bolivian and Chilean Salars. Aquat. Geochem. 15, 123–157.
Risacher, F., Alonso, H., Salazar, C., 2003. The origin of brines and salts in Chilean salars. A hydrochemical review. Earth Sci. Rev. 63, 249–293.
Ritter, B., Binnie, S.A., Stuart, F.M., Wennrich, V., Dunai, T.J., 2018. Evidence for multiple Plio_Pleistocene lake episiodes in the hyperaric Atacama Desert. Q. Geochronol. 44, 1–12.
Sáez, Al, Cabrera, L., Jensen, A., Chong, G., 1999. Late Neogene lacustrine record and palaeogeography in the Quillagua-Llamara basin, Central Andean fore-arc (northern Chile). Palaeogeogr. Palaeoclimatol. Palaeoevol. 151, 5–37.
Searl, A., Rankin, S., 1993. A preliminary petrographic study of the Chilean nitrates. Geol. Mag. 130 (3), 319–333.
Serpetzoglou, E., Albrecht, B.A., Kollias, P., Fairall, C., 2008. Boundary layer, cloud, and drzzle variability in the southeast Pacific stratocumulus regime. J. Clim. 21, 6191–6214.
Stern, C.R., 2004. Active Andean volcanism. Its geologic and tectonic setting. Rev. Geol. Chile 31, 161–206.
Suarez, M., 2009. A Late Mesozoic island arc in the southern Andes, Chile. Geol. Magaz. 116, 181–190.
Taussi, M., Godoy, B., Piscaglia, F., Morata, D., Agostini, S., Le Roux, P.J., Gonzalez-Maurel, O., Gallmeyer, G., Menzies, A., Renzulli, A., 2019. The upper crustal magma plumbing system of the Pleistocene Apacheta-Aguilucho Volcanic complex Area (Altiplano-Puna, Northern Chile) as inferred from the erupted lavas and their enclaves. J. Volcanol. Geotherm. Res. 373, 179–198.
Thiel, M., Macaya, E., Acuna, E., Arntz, W., Bastias, H., Brokordt, K., Camus, P., Castilla, J.C., Castro, L., Cortes, M., Dumont, C.P., Escribano, R., et al., 2007. The Humboldt current system of northern and central Chile. Oceanographic processes, ecological interactions and socioeconomic feedback. Oceanogr. Mar. Biol. 45, 195–334.
Thorpe, R.S., Potts, P.J., Francis, P.W., 1976. Rare Earth data and petrogenesis of andesite from the North Chilean Andes. Contrib. Mineral. Petrol. 54, 65–78.
Trumbull, R., Riller, U., Oncken, O., Scheuber, E., Munier, K., Hongn, F., 2006. The Time-Space distribution of Cenozoic Volcanism in the South-Central Andes. A new data compilation and some tectonic implications. Front. Earth Sci. 29–43.
Van Moort, J.C., 1985. Natural enrichment processes of nitrate, sulphate, chloride, iodate, borate, perchlorate and chromate in the caliche of northern Chile. Congr. Chil. 4 (3), 674–702.
Vásquez, P., Sepulveda, F., Quezada, A., Aguilef, S., Franco, C., Blanco, N., 2018. Cartas Guanillos del Norte y Salar de Llamara, Regiones de Tarapaca y Antofagasta, eds., Carta Geologica de Chile, Serie Geologica Basica, pp. 1–93.
Victor, O., Oncken, J. Glodny, 2004. Uplift of the western Altiplano plateau. Evidence from the Precordillera between 20° and 21°S (northern Chile). Tectonics 23, 4.
Voigt, C., Klipsch, S., Herwartz, D., Chong, G., Staubwasser, M., 2020. The spatial distribution of soluble salts in the surface soil of the Atacama Desert and their relationship to hyperaridity. Global Planet. Change 184.
Wang, F., Michalski, G., Seo, J., Ge, W., 2014. Geochemical, isotopic and mineralogic constraints on atmospheric deposition in the hyper-arid Atacama Desert, Chile. Geochim. Cosmochim.Acta 2014.
Wittenbrink, R., 1997. Temporal Variations of the Magma Genesis of Miocene and Quaternary Volcanic Rocks in the Southern Part of the Central Volcanic Zone of the Andes (CVZ, 25°-26°S, 67°-69°W). Berliner Geowiss. Abh. A 193, 1–135.
Wood, R., Mechoso, C.R., Bretherton, C.S., Weller, R.A., Huebert, B.J., et al., 2011. The VAMOS ocean-cloud-atmosphere-land study regional experiment (VOCALS-Rex) gaols, platforms, and field operations. Atmos. Chem. Phys. 11, 627–654.
Wörner, G., Lopez-Escobar, L., Moorbath, S., Horn, S., Entenman, J., Harmon, R.S., Davidson, J.D., 1992. Local and regional geochemical variations in the quaternary volcanic front of the central Andes (17° 30′ – 22° 00' S) Northern Chile. Rev. Geol. Chile 37–59.
Zinelabedin, A., Ritter, B., Joel, M., Dunai, T.J., 2024. Testing Calcium sulphate-wedge formation in deposits from the Aroma alluvial fan as indicator for haloturbation in the Atacama Desertt. The potential of using coarse-grain feldspars for post-IR IRSL dating of calcium sulphate-wedge growth in the Atacama Desert. Q. Geochronol. 71.